

Subtropical drying under greenhouse gas-induced warming

Jian Zhu^{1,4} · Aiguo Dai² · Danqing Huang^{3,5} · Xiucheng Xiao⁶ · Yuting Liu³

Received: 4 June 2022 / Accepted: 16 April 2023 © The Author(s), under exclusive licence to Springer-Verlag GmbH Germany, part of Springer Nature 2023

Abstract

Precipitation increases under increasing greenhouse gases (GHGs) over the globe, except many subtropical areas where it decreases. Several mechanisms have been proposed to explain this subtropical drying, which increases the risk of drought over subtropical land areas but was considered as a temporary response to increased GHGs by a recent study. Here climate simulations by different models under different forcing scenarios, including three multi-millennium simulations, are analyzed to examine the changes in the boundaries, area and mean precipitation of the subtropical dry zones, defined as the areas with annual-mean precipitation (P) below 2.5 mm/day. Results show that dry-zone mean P decreases under all forcing scenarios, over all time periods and persists into new equilibrium states. After the initial transient period, the northern and southern dry-zone boundaries of the Northern Hemisphere shift poleward and equatorward respectively, while those of the Southern Hemisphere mainly shift equatorward. During the initial transient period, the dry-zone boundaries expand both equatorward and poleward, consistent with previous studies. Dry-zone areas of both hemispheres increase. In contrast, mean precipitation averaged over subtropical subsidence zones may increase due to increased water vapor and weak drying over areas with weak subsidence. Increased subtropical subsidence and decreased subtropical precipitation are associated with increased equator-subtropical sea surface temperature gradients, which may lead to increased dry-zone area. Particularly, the P decreases over the subtropical dry zones result mainly from the enhanced drying effect due to increased vertical gradient of water vapor (dq/dz), with additional drying from increased subsidence, but offset by the wetting effect of increased water vapor. The dq/dz change results from tropospheric warming that persists throughout all stages of GHG-induced warming, which explains why the subtropical drying is a permanent response to GHG increases.

Keywords Subtropical dry zone · GHG induced-warming · SST gradient · Vertical gradient of water vapor

- ☐ Danqing Huang huangdq@nju.edu.cn
- College of Hydrology and Water Resources, Hohai University, Nanjing 210098, China
- Department of Atmospheric and Environmental Sciences, University at Albany, State University of New York (SUNY), Albany, NY 12222, USA
- School of Atmospheric Sciences, Nanjing University, Nanjing 210023, China
- ⁴ China Meteorological Administration Hydro-Meteorology Key Laboratory, Nanjing 210098, Jiangsu, China
- Frontiers Science Center for Critical Earth Material Cycling, Nanjing University, Nanjing 210023, China
- Fujian Climate Center, Fujian Meteorological Bureau, Fuzhou 350007, China

Published online: 30 April 2023

1 Introduction

As Earth's climate warms in response to rising greenhouse gases (GHGs), even with some uncertainties, precipitation is expected to increase over most of the globe, except many subtropical dry regions where precipitation is projected to decrease (He and Soden 2016; Scheff and Frierson 2012a, b; Delworth and Zeng 2014; Dai et al. 2018; Huang et al. 2020). This subtropical drying greatly increases the risk of drought over many subtropical land areas (Dai et al. 2018). In contrast to this projected subtropical drying under current global warming, paleoclimate proxy data suggest wetter subtropics than today during the warm early-middle Pliocene about 3–4 Mya (Burls and Fedorov 2017), when the orbital forcing and atmospheric CO₂ level were essentially the same as today, with atmospheric CO2 around 400 ppm (Fedorov et al. 2013). This differs from today's dry subtropics and is inconsistent with the projected decreases in subtropical



precipitation in the twenty-first century under GHG-induced warming. Thus, there is an apparent contradiction among the early-middle Pliocene warm and wet subtropics and today's warm and dry subtropics and the projected even warmer and drier subtropics in the twenty-first century. However, we should emphasize that the early-middle Pliocene climate represents an equilibrium state, while today's and the projected twenty-first century climates are transient states. This raises the question: Is the current and projected subtropical drying only a temporary and transient response to the GHG forcing or will it persist into the final state as the system approaches a new equilibrium?

Sniderman et al. (2019) suggested that the projected Southern Hemisphere subtropical drying in the twenty-first century may be only a temporary response to GHG-induced rapid warming that may disappear as the system reaches a new equilibrium. Their main evidence is that the negative precipitation change averaged over 25°S–35°S weakens during the twenty-second and twenty-third centuries compared with that in the twenty-first century and its annual precipitation change is either small or become positive in the twenty-third century in the simulations under the Extended Concentration Pathway 8.5 and 4.5 (ECP8.5 and ECP4.5) by nine CMIP5 models. However, the 25°S-35°S zone includes many wet areas with annual precipitation exceeding 2-3 mm/ day (such as over South America and many oceanic areas), where future precipitation increases. Thus, the mean precipitation change averaged over the entire 25°S-35°S zone is not representative of that over the Southern Hemisphere subtropical dry zone defined by climatological annual-mean precipitation amount. Furthermore, the twenty-third century change examined by Sniderman et al. (2019) is still a transient response to the external forcing of the earlier and twenty-third centuries; therefore, it does not allow the authors to make conclusions regarding the equilibrium response. Thus, how the subtropical dry zones change under GHG-induced transient or equilibrium warming is still an open question.

Our recent work (Huang et al. 2020) showed that the spatial change patterns of surface air temperature (SAT) and precipitation are similar and stable at different warming stages and under different forcing scenarios when the patterns are normalized into local change per 1 K global warming. In particular, Huang et al. (2020) showed that the subtropical drying will persist into the near-equilibrium states reached 3000–5000 years after an abrupt quadrupling of atmospheric CO₂ in several models. Thus, it is unlikely that the subtropical drying is only a temporary phenomenon that exists only during the transient response period. This depends on the evolution of the meridional SST gradient with time and whether it weakens enough for the dynamic effect to overcome the thermodynamic effect. This suggests that the inconsistency between the early-middle Pliocene

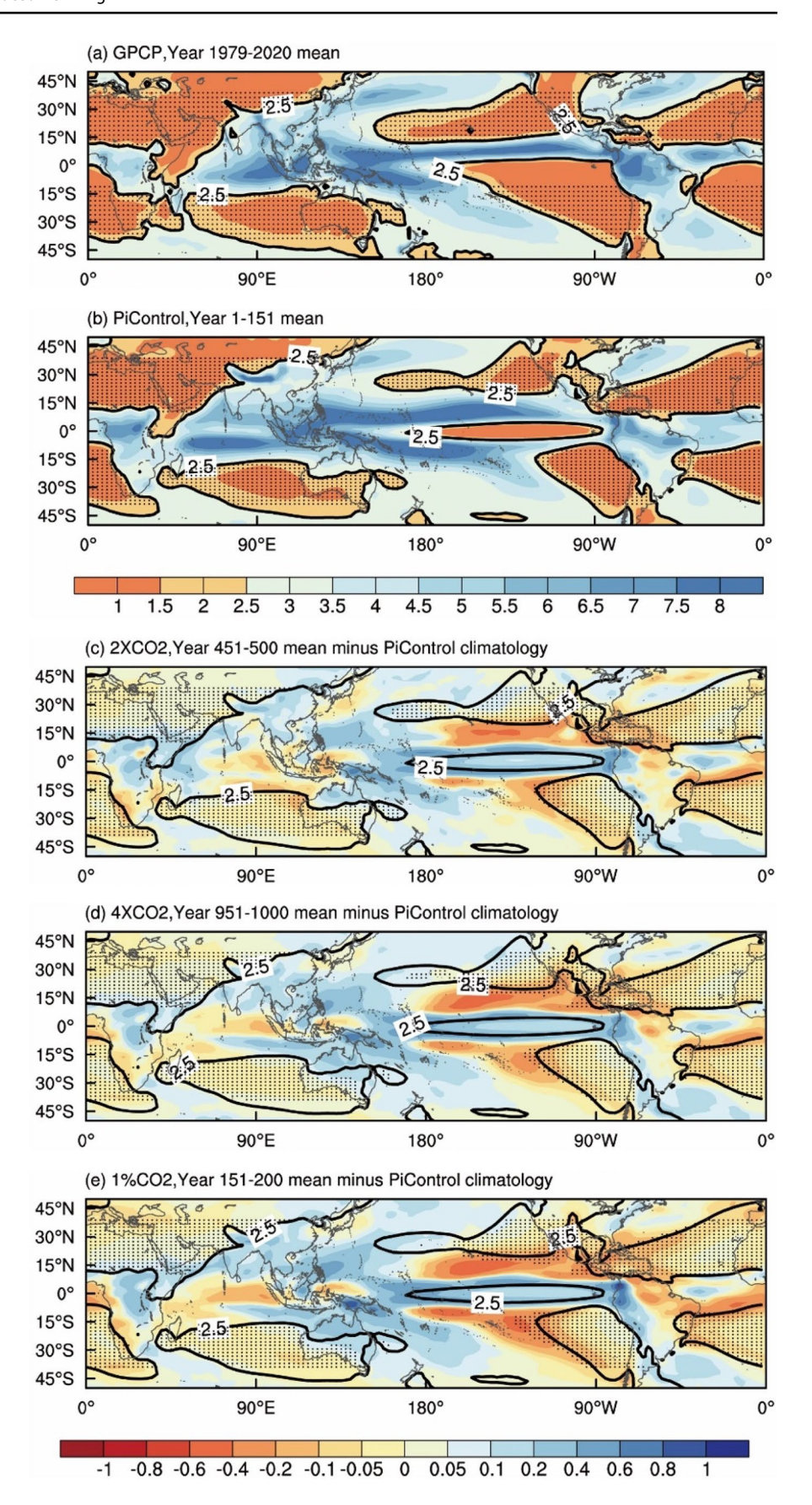
warm and wet subtropics and today's and near-future warm and dry subtropics cannot be explained by the small differences between the transient and equilibrium change patterns simulated by current climate models. However, as their focus is on global change patterns, Huang et al. (2020) did not specifically examine the time-dependent response of the subtropical dry zones (in terms of its northern and southern boundaries and its area) and their mean precipitation and subsidence under various warming scenarios.

The subtropical dry zones is usually defined by the regions where annual precipitation minus annual evaporation is less than zero (Seager et al. 2010; Scheff and Frierson 2012b), or equivalently by combining annual precipitation with annual potential evapotranspiration to define aridity over land (Feng and Fu 2013). Furthermore, many studies used the zero line of the zonal-mean mass flux stream-function to define the edges of the subtropical subsidence zones and found a poleward expansion of these zones (e.g., Lu et al. 2007; Fu and Lin 2011; Davis and Birner 2017), which is often linked to the expansion of the Hadley Cell found in observations (Hu and Fu 2007) and model projections (Lu et al. 2007; Gastineau et al. 2008; Hu et al. 2013; Tao et al. 2016). Scheff and Frierson (2012a, b) found that most of the CMIP3 and CMIP5 model-simulated precipitation decreases are located poleward of the latitude location of the current subtropical zonal-mean precipitation minimum (ϕ_{min}), from which they concluded that the model-simulated subtropical drying results mainly from a poleward expansion of the subtropical dry zones. However, as the current subtropical dry zones cover a large area poleward of ϕ_{min} , it is possible that many of the projected precipitation decreases may still be within the current dry zone, rather than outside of it due to its expansion, as shown by Fig. 1a-b of Dai et al. (2018). That is, the relative locations of the projected precipitation change and ϕ_{min} do not really allow one to infer about the areal change of the subtropical dry zones; one needs to examine the changes in the actual boundaries of the dry zone, which is usually defined based on long-term annual-mean precipitation (Huang et al. 2017a). Because future subtropical precipitation will be influenced by not only subsidence but also increases in atmospheric water vapor, the dry zone defined by annual-mean precipitation (P) may differ from the subsidence zone examined by Lu et al. (2007) and others. Thus, from these earlier studies, which examined only transient responses, it is still unclear whether the subtropical dry zones (defined in terms of P) will expand poleward under GHG-induced warming and whether such a change will be just a transient response or will persist into a new equilibrium state.

Several mechanisms have been proposed to explain the subtropical drying; they include enhanced drying by subsidence due to the negative horizontal temperature advection and increased vertical gradients of specific humidity



Fig. 1 Annual-mean precipitation climatology (in mm/day) from (a) GPCP v2.3 observational data (Adler et al. 2018) averaged over years 1979-2020, (b) the CESM1 PiControl run (for years 1-151), and its normalized change [as the CESM1simulated change (relative to the PiControl climatology and averaged over the last 50 years) divided by the global-mean temperature change, in mm/day per 1 K global warming] from CESM1 (c) $2 \times CO_2$ (for years 451-500), (**d**) $4 \times CO_2$ (for years 951-1000) and (e) 1% CO₂ (for years 151-200) simulations. The 2.5 contour outlines the current areas with annual-mean precipitation below 2.5 mm/day in GPCP in (a) and in CESM1 PiControl run in (b-e). The dots indicate the subtropical dry zones with annual-mean precipitation below 2.5 mm/ day within 10°S-40°S and 10°N-40°N in GPCP in (a) and in each experiment for the stated time period in other panels





(Chou et al. 2009), poleward expansion of the subtropical subsidence zones (Lu et al. 2007) and poleward shifts of the subtropical dry zones (Scheff and Frierson 2012a, b), increased regional land-sea thermal contrast (He and Soden 2016), increased horizontal moisture transport (Held and Soden 2006), and changes in meridional SST gradients over the equatorial Pacific (Burls and Fedorov 2017). Different precipitation responses to GHG forcing over the subtropical and other oceans have also been attributed to the different change patterns in SSTs (Xie et al. 2010). In particular, the meridional (tropical to subtropics) SST gradients may affect the strength of the Hadley circulation and thus precipitation in the deep tropics and the subtropics (Xie et al. 2010; Fedorov et al. 2015; Burls and Fedorov 2017). The SST and SAT change patterns averaged over a few to several decades may be significantly influenced by internal climate variability (Dai et al. 2015; Dong and Dai 2015), which can contribute to regional SST and precipitation differences averaged over such periods among individual model projections that contain different realizations of internal variability. One way to minimize such influence by realization-dependent internal variability is to compare the averages over many decades (e.g., 50-100 years; Huang et al. 2020, 2022; Liu et al. 2022) or over many ensemble simulations (Dai and Bloecker 2019).

Here, we use long-term simulations with the Community Earth System Model version 1 (CESM1; Hurrell et al. 2013), together with the extended multi-century simulations from CMIP6 experiments and the abrupt $4 \times CO_2$ multi-millennium simulations from three climate models, to address the following questions:

- 1. How do the northern and southern boundaries of the subtropical dry zones (defined using a threshold of annual-mean precipitation) change under GHG-induced transient and equilibrium global warming?
- 2. What are the possible mechanisms behind the model-projected changes in the intensity and size of subtropical dry zones? and,
- 3. How do the changes for the subtropical drying zones compare with those for the subtropical subsidence zones under GHG-induced global warming?

Answers to these questions should improve our understanding of the response of the subtropical dry zones to GHG forcing. They may also help us understand the warm and wet subtropics during the early-middle Pliocene. Our study differs from previous studies (e.g., Lu et al. 2007; Scheff and Frierson 2012a, b; Feng and Fu 2013; Davis and Birner 2017) in that we focus on the actual boundaries of the subtropical dry zones defined by local annual-mean precipitation, rather than the subsidence zone or precipitation change patterns; and we also compare the transient and equilibrium

changes using multi-millennial long simulations. In contrast, the previous studies only examined recent or near-future transient changes of the dry zone under increasing GHGs and they did not explicitly explore the key mechanisms or processes leading to the precipitation decreases within the interior of the current dry zone and over the newly expanded dry-zone areas.

2 Model experiments and analysis method

We address the above questions by analyzing three groups of experiments summarized in Table 1. First, we ran long simulations with the Community Earth System Model version 1.2.1 (CESM1) (Hurrell et al. 2013) for three experiments: a 500-year run with abrupt CO_2 doubling $(2 \times CO_2)$ of the pre-industrial CO₂, a 1000-year run with abrupt CO₂ quadrupling $(4 \times CO_2)$, and a 235-year run with 1% CO_2 increase per year (1% CO₂) starting from the pre-industrial level of 284.7 ppm. The climatology from a 151-year pre-industrial control run (PiControl) using the CESM1 was used as the baseline for computing changes for the experiments with increased GHGs. Detailed descriptions about these CESM1 simulations are provided in Huang et al. (2020). Second, we used the historical plus extended SSP5-8.5 simulations from 1850 to 2300 available from six CMIP6 (Eyring et al. 2016) models (namely, ACCESS-CM2, ACCESS-ESM1-5, CanESM5, CESM2-WACCM, IPSL-CM6A-LR, and MRI-ESM2-0). Please note that most CMIP6 models do not provide simulations beyond 2100; thus, they are not ideal for analyzing long-term responses. Third, we analyzed data from abrupt 4×CO₂ multi-millennium simulations from three coupled models (MPI-ESM-1.1, GISS-E2-R, and CESM 1.0.4) obtained from https://data.iac.ethz.ch/longr unmip/ and described in Rugenstein et al. (2019). The longterm climatology from the PiControl runs by these three models was used as the baseline for computing the changes. More details about these experiments are shown in Table 1. In this study, following Huang et al. (2020), all the changes are normalized by the global-mean warming amount relative to the pre-industrial control run and expressed as changes per 1 K global warming; this minimizes the impact by different global warming amounts due to different radiative forcing under different scenarios or during different time periods.

In this study, one of our goals is to determine whether the subtropical precipitation decrease is only a temporary or transient response to increased GHGs, or it is persistent into the new equilibrium climate. Here, we refer to the precipitation decrease as drying, which does not refer to the drying of the land surface. The latter can be caused by precipitation decreases, potential evapotranspiration increases, or both, which is the case in the subtropics (Dai et al. 2018). Thus,



Table 1 The model simulations used in this study

Model name	Institution (Country)	Experiments (years)	Lon×Lat
	CESM1 simulations		
CESM1.2.1	National Center for Atmospheric Research (USA)	$2 \times CO_2$ (500 years)	144×96
		$4 \times CO_2$ (1000 years)	
		1% CO ₂ (235 years)	
		PiControl (151 years)	
	CMIP6 model simulations		
ACCESS-CM2	Commonwealth Scientific and Industrial Research Organisation (Australia)	Historical (year 1850-2014)	192*144
	Australian Research Council Centre of Excellence for Climate System Science (Australia)		
ACCESS-ESM1-5	Commonwealth Scientific and Industrial Research Organisation (Australia)		192*145
CanESM5	Canadian Centre for Climate Modelling and Analysis (Canada)	SSP5-8.5 (year 2015–2300)	128×64
CESM2-WACCM	National Center for Atmospheric Research (USA)		288×192
IPSL-CM6A-LR	Institute Pierre-Simon Laplace (France)		144×143
MRI-ESM2-0	Meteorological Research Institute (Japan)		320×160
	Long simulations with abrupt 4×CO ₂		
MPI-ESM-1.1	Max Planck Institute for Meteorology (Germany)	$4 \times CO_2$ (4458 years)	192×96
		PiControl (2000 years)	
GISS-E2-R	NASA Goddard Institute for Space Studies (USA)	$4 \times CO_2$ (5000 years)	144×90
		PiControl (5225 years)	
CESM1.0.4	National Center for Atmospheric Research (USA)	$4 \times CO_2$ (5900 years)	144×96
		PiControl (1000 years)	

following previous studies (Huang et al. 2017a, b), we define the subtropical dry zones within 10°S-40°S and 10°N-40°N using individual grid boxes whose long-term (e.g., 50-year) annual-mean precipitation is below 2.5 mm/day (Fig. 1). This allows us to examine the temporal changes in the actual boundaries and areal extent of the dry zone in model simulations. We analyze the Northern Hemisphere (N.H.) and Southern Hemisphere (S.H.) dry zones separately, focusing on changes in their southern and northern boundaries, area, mean precipitation and vertical velocity, and their underlying mechanisms. We choose the 2.5 mm/day threshold after testing different thresholds (e.g., 1.5, 2.0 and 3.0 mm/day) for defining the subtropical dry zones. We found that using observational precipitation data from GPCP v2.3 (Adler et al. 2018), the 2.5 mm/day threshold can best identify the well-known subtropical dry regions, while a 3.0 mm/day threshold results in subtropical dry zones that almost covers the entire subtropical regions. Because the poleward boundary may reach 40°N/S (the edge of the predefined subtropics) at some locations, especially at the northern boundary in Eurasia and western North America, which may affect the boundary change, we employed two ways to examine the issue. First, we set the northern edge of the N.H. subtopic as 45°N and recalculated the boundary changes. The results showed a similar but more obvious equatorward shift of the northern boundary in the N.H. (figure not shown). Second, we chose lower thresholds (1.5 and 2.0 mm/day). A 2.0 mm/

day threshold leads to slightly smaller but similar subtropical dry zones, as shown previously (Dai et al. 2018). Moreover, a 1.5 mm/day threshold leads to the dry-zone boundaries getting farther away from the edges of the subtropics, and their changes show similar shifts as shown in Fig. 7a–d. The dry-zone changes are not very sensitive to the thresholds used to define the dry zone. Overall, even though the boundary at certain locations reaches the predefined edges of the subtropics in our original definition, our results are not greatly affected by this limitation.

To explore possible links between the subtropical dry zones, subtropical pressure vertical velocity (ω , positive downward), and the tropical-subtropical SST gradient (referred to as meridional temperature gradient or MTG), we define the subtropical-mean vertical velocity and MTG as follows:

$$\omega_{N.H.} = \left[\langle \omega \rangle \right]_{(10^{\circ}-40^{\circ}\,\mathrm{N})},$$

$$\omega_{S.H.} = [\langle \omega \rangle]_{(10^{\circ} - 40^{\circ} \text{ S})}$$

$$MTG_{N.H.} = [SST]_{(0^{\circ}-10^{\circ} \text{ N})} - [SST]_{(10^{\circ}-40^{\circ} \text{ N})},$$

$$MTG_{S.H.} = [SST]_{(0^{\circ}-10^{\circ} \text{ S})} - [SST]_{(10^{\circ}-40^{\circ} \text{ S})},$$



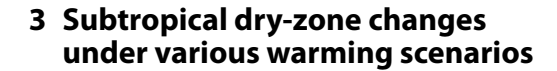
where the square brackets denote the zonal averaging over 0° –360° longitudes and over the indicated latitude bands, and the angle brackets " $\langle \rangle$ " indicate averaging vertically from 700 to 300 hPa (the mid-troposphere, following Byrne et al. 2018). We also examined latitude bands of 25°–35°N, 20° –40°N, 25° –35°S and 20° –40°S as the subtropics, and the results are not very sensitive to this latitude band.

To help understand what induces changes in subtropical dry-zone precipitation, the vertically integrated moisture budget (Chou et al. 2009),

$$P' = -\left\langle \overline{\omega} \partial_p \mathbf{q}' \right\rangle - \left\langle \omega' \partial_p \overline{\mathbf{q}} \right\rangle - \left\langle \vec{V} \cdot \nabla \mathbf{q} \right\rangle' + E' + \varepsilon, \tag{1}$$

is further diagnosed, where the overbar denotes the PiControl climatology (for the CESM1) or 1900–1999 mean (for CMIP6 historical runs), which is defined as the current climate. Here (') represents the departure or change from the current climate, " () "denotes vertical mass integration from 1000 to 500 hPa, as the upper levels do not directly contribute to low-level convergence and thus precipitation, ∂_n represents the vertical derivative with respect to pressure, P is precipitation, q is specific humidity, E is local surface evaporation, and ε is a residual term. Chou et al. (2009) revealed that the first two terms $-\langle \overline{\omega} \partial_n q' \rangle$ (referred to as P1) and $-\langle \omega' \partial_n \overline{q} \rangle$ (referred to as P2) on the right side of Eq. (1) are most important, they represent the contributions from changes in vertical moisture transport or convergence (a thermodynamic term) associated with mean flow $(\overline{\omega})$ and changes in the vertical gradient of water vapor $(\partial_n q')$ and from changes associated with changes in vertical velocity $(\omega', a \text{ dynamic term})$ and the mean water vapor gradient $(\partial_n \overline{q})$, respectively. To quantify the thermodynamic effect from increased water vapor only through horizontal water vapor transport or convergence, in the 3rd term $(-\langle \vec{V} \cdot \nabla q \rangle)$, referred to as P3), we used the PiControl

 \vec{V} (horizontal winds) to exclude its future change and emphasize the role of changes in water vapor horizontal gradients, so that P3 represents the contribution of water vapor only through horizontal gradient changes without wind changes. Note that the effect of increased water vapor through vertical convergence is included in P1, and changes in horizontal wind convergence are included through ω' in P2. To understand the relative importance of the budget terms in Eq. (1) for the subtropical precipitation changes, the 4th term E' (referred to as E), which is the change in local surface evaporation, is also examined for the CMIP6 experiments.



We first examine how the subtropical dry zones change among different simulations. Figure 1 shows the current annual-mean precipitation maps and the subtropical dryzone areas outlined by the 2.5 mm/day contour from GPCP observational data and CESM1 PiControl run, together with their changes in the CESM1 $2 \times CO_2$, $4 \times CO_2$ and 1% CO_2 experiments. The GPCP data (Fig. 1a) show that the lowprecipitation areas are located mainly over the subtropical eastern South and North Pacific and Atlantic Oceans, Australia, the southern Indian Ocean, southern and northern Africa, the Mediterranean region, the Middle East, and western North America. The CESM1 PiControl run (Fig. 1b) broadly reproduces these low-precipitation areas, albeit with noticeable differences (e.g., unrealistic dry zone over the equatorial central-eastern Pacific due to the cold tongue biases of SST). Here we will focus only on the low-precipitation areas within 10°-40°N or S and refer to them as the subtropical dry zones (indicated by dotted areas in Figs. 1, 2, 3). The subtropical dry zones in the historical simulations by the six CMIP6 models (Fig. 2) and the PiControl runs (Fig. 3) by the three models with abrupt $4 \times CO_2$ multi-millennium simulations show patterns broadly similar to those in GPCP. Thus, these models simulate the subtropical dry zones reasonably well.

The subtropical dry zones (indicated by dots in Figs. 1, 2, 3) are relatively stable with only small changes among all the model simulations under different warming scenarios, with decreased precipitation over most of the dry zone areas. Most of these GHG-forced simulations (Figs. 1, 2, 3) show large precipitation decreases over regions to the south of the current subtropical North Pacific dry zone and to the west of the current subtropical South Pacific dry zone. It is evident that the boundaries and area of the subtropical dry zones change noticeably in some of the simulations (e.g., Figs. 1d, e, 2b, d, h, l, 3d, f).

To illustrate the temporal evolution of the subtropical dry zones under increasing GHGs, we show the time series of the subtropical dry-zone boundaries, area and mean precipitation under various warming scenarios in Figs. 4, 5, 6, 7. We notice that the subtropical dry-zone edges over Eurasia and a few other regions reach or exceed 40°N/S (Figs. 1, 2, 3), thus our poleward changes of the dry zone reflect the edge shifts within 40°N/S but excludes those outside it. This is reasonable since our focus is on changes in the subtropical dry zones, rather than the changes in midlatitude dry areas, and the 40°N/S limits already provide enough room for subtropical dry-zone boundary changes in future climates. We checked those poleward boundaries reaching the 40°N/S limits and found that they mostly move equatorward, which



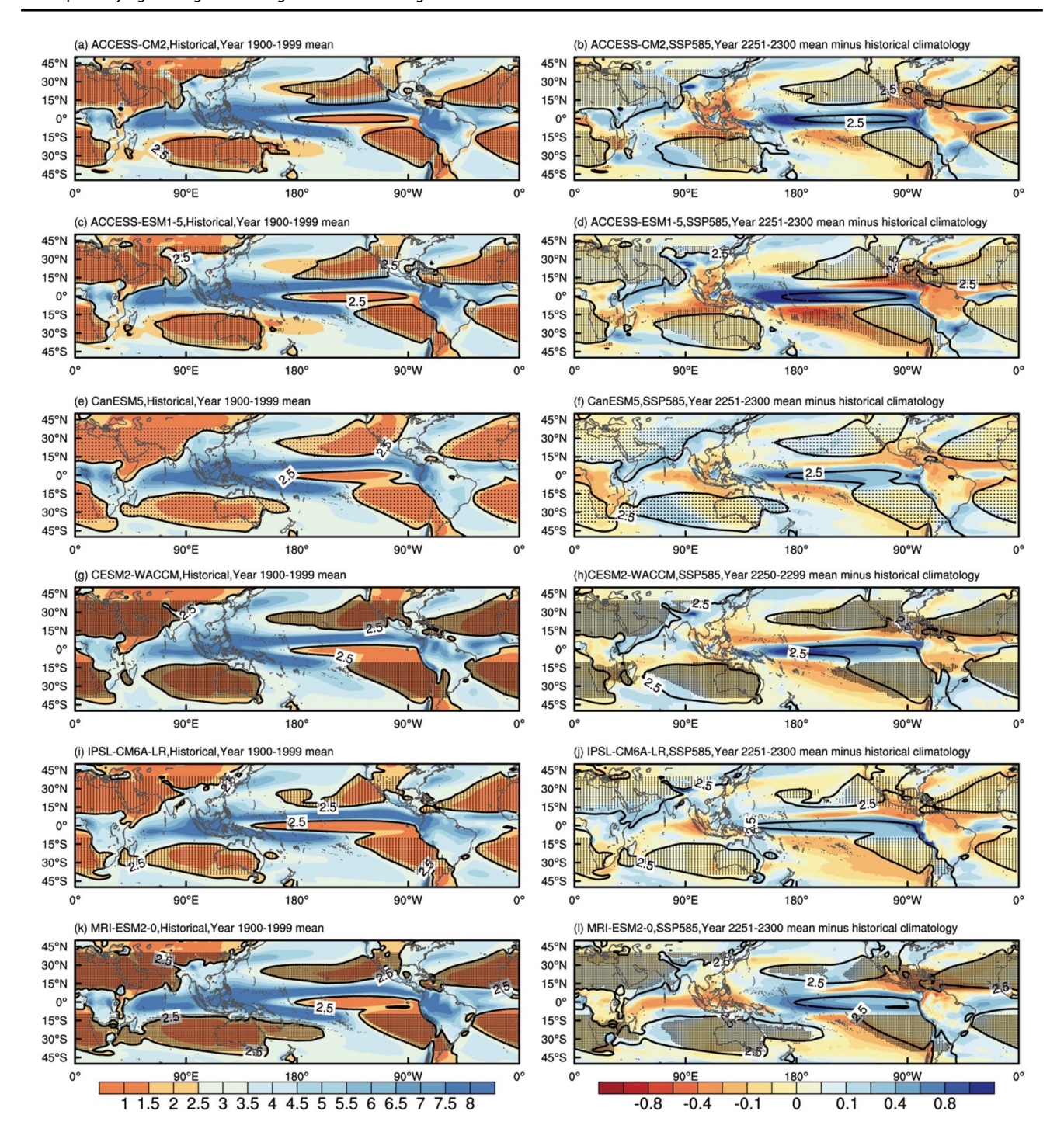


Fig. 2 Annual-mean precipitation (in mm/day) from the six CMIP6 models in (**a**, **c**, **e**, **g**, **i**, **k**) their historical run (average over years 1900–1999) and (**b**, **d**, **f**, **h**, **j**, **l**) its normalized change [as the differences between 2251–2300 (under SSP5-8.5) and 1900–1999 (under historical forcing) divided by the global-mean temperature change, in mm/day per 1 K global warming] for (**a**, **b**) ACCESS-CM2, (**c**, **d**) ACCESS-ESM1-5, (**e**, **f**) CanESM5, (**g**, **h**) CESM2-WACCM, (**i**, **j**)

IPSL-CM6A-LR, and (k, l) MRI-ESM2-0. The 2.5 contour outlines the current areas with annual-mean precipitation below 2.5 mm/day in each historical run. The dots indicate the historical (left panels) and future (right panels) subtropical dry zones with annual-mean precipitation below 2.5 mm/day within 10°S-40°S and 10°N-40°N in each experiment for the stated time period



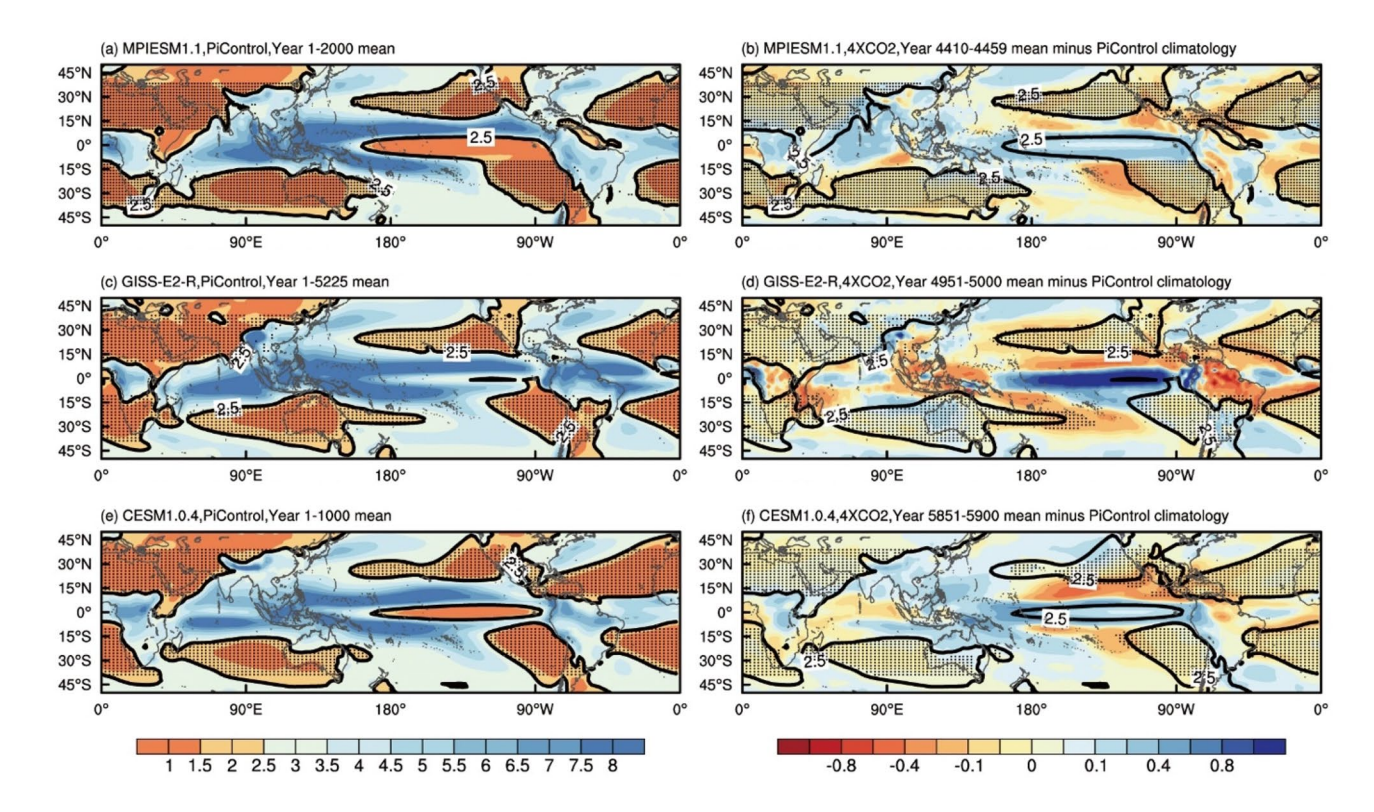


Fig. 3 Annual-mean precipitation (in mm/day) from $\bf a, c, e$ the PiControl climatology and $\bf b, d, f$ the its normalized change [as the change (relative to the PiControl climatology) over the last 50 years of the multi-millennial $4\times CO_2$ simulation divided by the global-mean temperature change, in mm/day per 1 K global warming] for $\bf a, b$ MPI-ESM-1.1, $\bf c, d$ GISS-E2-R, and $\bf e, f$ CESM1.0.4. The 2.5

contours for the mean precipitation outline the current areas with annual-mean precipitation below 2.5 mm/day in the PiControl run. The dots indicate the PiControl (left panels) and future (right panels) subtropical dry zones with annual-mean precipitation below 2.5 mm/day within 10°S–40°S and 10°N–40°N in each experiment for the stated time period

means most of the boundary changes will not be affected by the 40°N/S limits (figure omitted). For the N.H. dry zone, the CESM1 experiments consistently show a southward shift of the southern boundary (by $\sim 0.2^{\circ}-0.6^{\circ}$ latitude per 1 K global warming) with a small northward shift of the northern boundary (by $\sim 0.05^{\circ}$ –0.2° latitude per 1 K global warming) under the $2 \times CO_2$, $4 \times CO_2$ and $1\% CO_2$ forcing scenarios (Fig. 4a), leading to increased dry-zone area (by $\sim 0.5-2.5\%$ per 1 K global warming, Fig. 4c, except some larger changes in the first 50 years, especially for the 1% CO₂ run). In contrast, for the S.H. dry zone, only the northern boundary expands northward (by ~0.1°-0.2° latitude per 1 K global warming), while the southern boundary either changes little or moves slightly northward (Fig. 4b). Despite this, the S.H. dry-zone area still increases considerably (by $\sim 0.5-5\%$ per 1 K global warming, Fig. 4d, except some larger changes in the first 50 years), which is partly due to westward expansion of the dry zone in the eastern South Pacific (e.g., Fig. 1c-e). Thus, the subtropical dry zones expand mainly equatorward after the initial transient period, especially for the low-latitude dry-zone boundaries.

The mean precipitation over the time-varying subtropical dry zones decreases in both hemispheres, especially in the N.H. (by $\sim 1-5\%$ per 1 K global warming, except some larger changes in the first 50 years) under GHG-induced warming (Fig. 4e, f). These decreases exist throughout the long $2 \times CO_2$ and $4 \times CO_2$ simulations, suggesting that the subtropical drying in both hemispheres is not a temporary and transient response to increased GHGs. In Fig. 4, The large percentage changes per 1 K global warming in the first 50 years in the 1% CO₂ run are mainly due to the division by the small warming amounts during the first several decades. The 31-year smoothed changes from the 1% CO₂ run approach the steady levels seen in the $2 \times CO_2$ and $4 \times CO_2$ simulations, although some multidecadal-centennial fluctuations exist, especially for the dry-zone area. This suggests that (a) internal variability can significantly influence the estimated dry zone (its boundaries, area, and mean precipitation) using data over a short time period (e.g., <50 years); (b) the normalized dry-zone changes are similar in magnitude among different forcing scenarios; and (c) the subtropical drying induced by increased GHGs is permanent, not temporary.

The extended SSP5-8.5 simulations from the six CMIP6 models show diverse changes of the subtropical dry-zone boundaries (Fig. 5, red and pink curves). For example, for



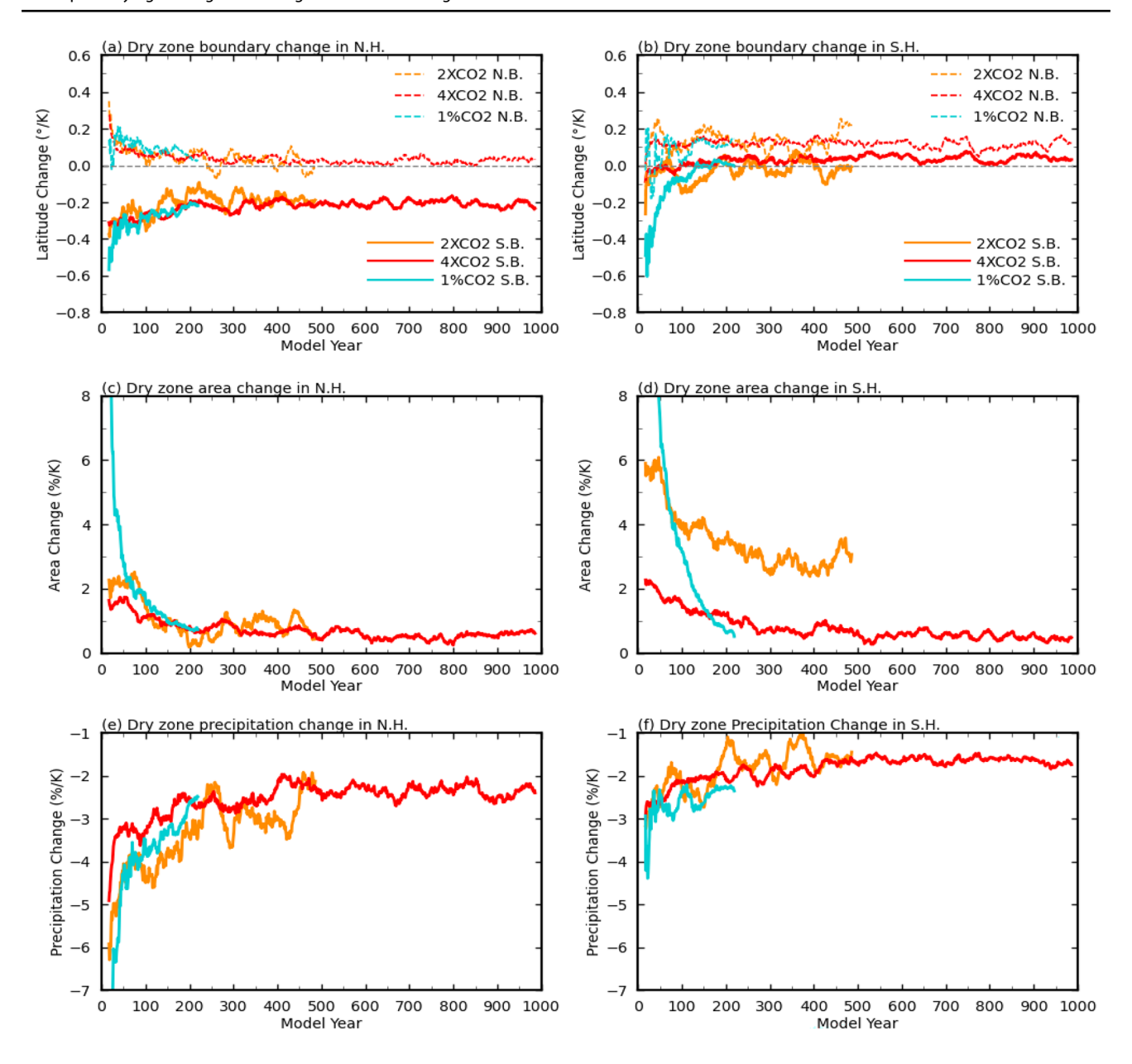


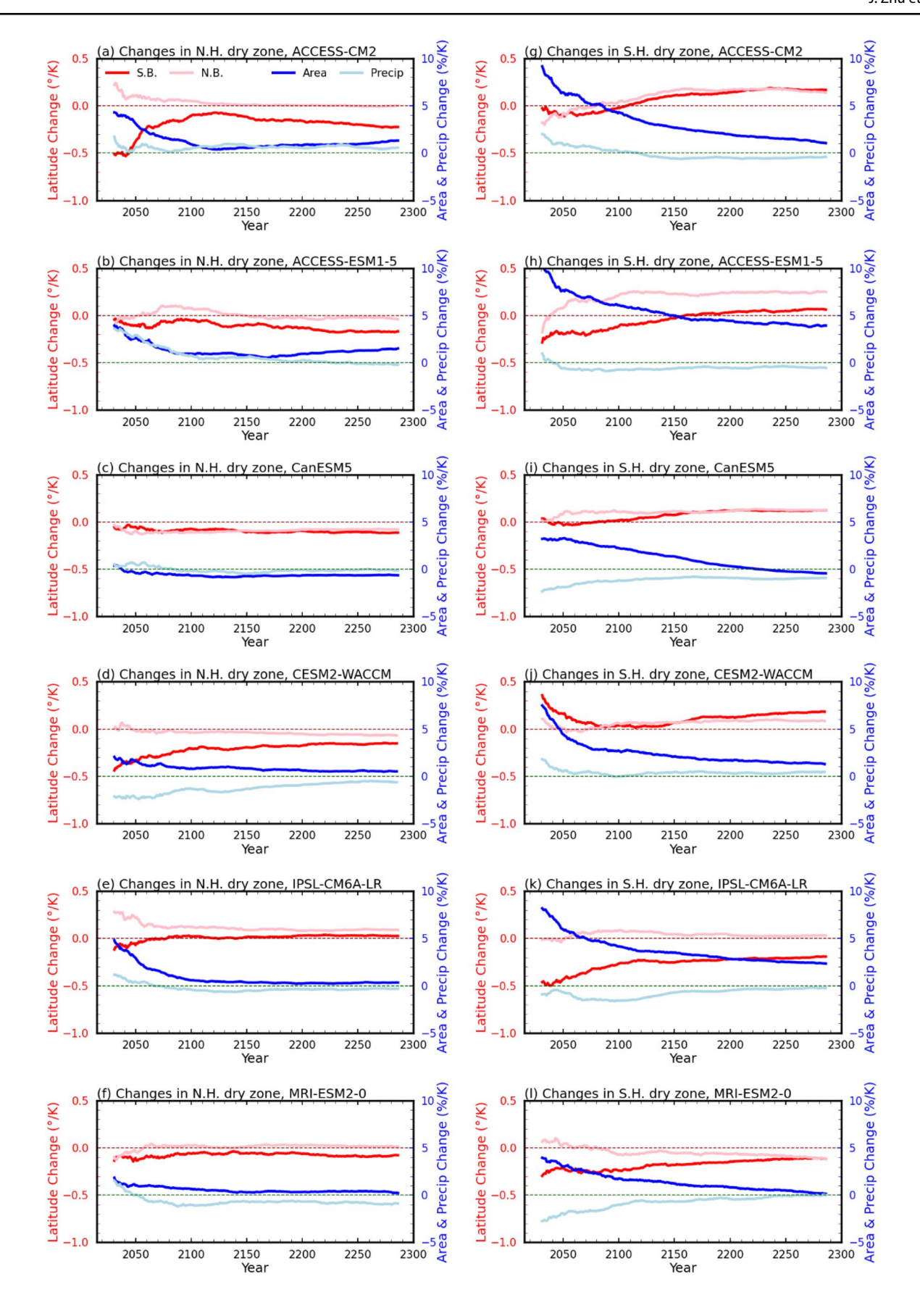
Fig. 4 Time series of the normalized 31-year moving averaged changes in subtropical dry-zone's southern boundary (S.B.) and northern boundary (N.B.) (**a**, **b** in degrees latitude per 1 K global warming), dry-zone area (**c**, **d** % change per 1 K global warming) and dry-zone mean precipitation (**e**, **f**, % change per 1 K global warming, averaged over the time-varying dry-zone area) in the Northern

Hemisphere (left panels) and Southern Hemisphere (right panels) for the three CESM1 experiments ($2\times CO_2$, $4\times CO_2$ and 1% CO_2). All the changes are relative to the PiControl run climatology. A positive latitude change means a poleward shift of N.H. dry zone boundaries and an equatorward shift of S.H. dry zone, vice versa for the negative change

the N.H. dry zone (Fig. 5a–f), the southern boundaries clearly show equatorward expansion in five models except IPSL-CM6A-LR, while the northern boundaries show slight equatorward expansion in four models except IPSL-CM6A-LR and MRI-ESM2-0. For the S.H. dry zone (Fig. 5g–l), the northern boundaries move equatorward in five models except MRI-ESM2-0, while the southern boundaries also show equatorward expansion in four models except IPSL-CM6A-LR and MRI-ESM2-0. For the dry-zone areas, they generally

increase in both hemispheres in most models; while for the dry-zone mean precipitation, it mainly decreases in most cases. Most of the normalized changes are steady over time, especially after the late twenty-first century. And the changes do not recover to their present values (i.e., zero change) for most cases. Overall, the CMIP6 model results are qualitatively consistent with the CESM1 in that they generally suggest an expansion of the subtropical dry-zone area and a decrease in subtropical dry-zone mean precipitation in both







∢Fig. 5 Time series of the normalized 31-year moving averaged changes in subtropical dry-zone's southern boundary (S.B.) and northern boundary (N.B.) (in degrees latitude per 1 K global warming, left y-axis), dry-zone area and dry-zone mean precipitation (% change per 1 K global warming, right y-axis) in the Northern Hemisphere (left panels) and Southern Hemisphere (right panels) from the CMIP6 SSP5-8.5 experiments using a, g ACCESS-CM2, b, h ACCESS-ESM1-5, c, i CanESM5, d, j CESM2-WACCM, e, k IPSL-CM6A-LR, and k, l MRI-ESM2-0. The red and blue dot lines indicate the zero lines for the red curves (left y-axis) and blue curves (right y-axis), respectively. All the changes are relative to the 1900–1999 mean from the historical runs. A positive latitude change means a poleward shift of N.H. dry zone boundaries and an equatorward shift of S.H. dry zone, vice versa for the negative change

hemispheres, albeit the dry-zone boundary changes differ among the CESM1 and CMIP6 simulations.

For the three multi-millennial $4 \times CO_2$ simulations, the CESM1.0.4 model shows mainly equatorward expansions of the subtropical dry zones with small changes for the poleward boundaries in both hemispheres, leading to increased dry-zone area with decreased dry-zone mean precipitation (Fig. 6c, f). These changes are very similar to our CESM1 results (Fig. 4), and they persist through the 5900-year simulations, again suggesting that these are permanent, not temporary, changes caused by the CO_2 increase. The subtropical dry-zone area (mean precipitation) also increases (decreases) permanently in the other two multi-millennial simulations, although the boundary expansion occurs mainly in the N.H. dry zone (Fig. 6a, b, d, e) and the dry-zone mean precipitation decrease is small in the S.H. in GISS-E2-R (Fig. 6e).

Figure 7 summarizes the normalized subtropical dryzone changes averaged over the last 50 years from all the experiments analyzed here. Most of the model simulations show an equatorward expansion of the dry zone in both hemispheres, while the changes for the high-latitude dryzone boundaries show more diverse shifts (Fig. 7a, b). All the cases show increased subtropical dry-zone area except CanESM5 (Fig. 7c), and decreased dry-zone mean precipitation except for the N.H. of ACCESS-CM2 and the S.H. of CESM2-WACCM (Fig. 7d). In general, the changes from the CESM1 experiments and the three multi-millennial simulations are in good agreement qualitatively, while the CMIP6 SSP5-8.5 simulations show diverse results, likely in part due to their transient nature and short length of simulation. We have further examined the changes in subtropical dry zones over land only as this is more societally relevant. The results show that both the northern and southern boundaries of the continental dry zones in both hemispheres' subtropics move mainly equatorward (Fig. 7e, h), and their changes are bigger than the subtropical dry zones. The continental dry zones do not show accordant increased area and weakened precipitation as the subtropical dry zones. More than half models show slightly decreased or increased area and strengthened or weakly increased precipitation for the N.H. dry zones.

Models show more spreads and some also show inconsistent changes between the two hemispheres. This may be partly due to the reduced areas of the continental dry zones, especially for the N.H..

The equatorward expansion revealed here differs from previous studies that suggested a poleward expansion of the subsidence zone (Scheff and Frierson 2012b) or a poleward (and equatorward) expansion of the Hadley Cell (Lu et al. 2007; Gastineau et al. 2008; Hu et al. 2013; Tao et al. 2016). These earlier studies examined the model-simulated transient changes during the twenty-first century. We examined the boundary changes of the N.H. and S.H. dry zones for different 50-year periods during the initial 300 years of the simulations analyzed here, and found that their boundaries expand both poleward and equatorward in the first 150 years but expand mainly equatorward thereafter (by comparing Fig. 8a, b and Fig. 7a, b). Thus, the likely reason for the discrepancy is that the earlier studies examined projections only up to about year 2100, which is still in the transient state, similar to the fast responses in the first 150 years shown in Figs. 4, 5, 6 and 8. Another factor is the positive effect of increased water vapor that may offset the negative effect of increased subsidence on precipitation over the poleward edges of the subsidence zone, which is examined in detail below in Figs. 9, 10.

Since descending motion suppresses formation of clouds and precipitation, we further use the 0 Pa/s contour of the vertical velocity (ω) at 500 hPa to define the subtropical subsidence zone, following Chou et al. (2009) and compare the subsidence-zone changes in its boundaries, area, and precipitation with the dry-zone changes discussed above. Figure 9 shows that the subtropical dry zones (black solid line) are generally located slightly inside the subtropical subsidence zones (green dashed line), but matches much better with the subsidence zones outlined by the contour of $\omega = 0.01$ Pa/s (blue dashed line) in the CESM1 PiControl run. The zonalmean changes in the boundaries, area and precipitation of the subtropical subsidence zones (Fig. 10a–d) differ substantially from those for the subtropical dry zones (Fig. 7a–d). Precipitation decreases over many parts of the subtropical subsidence zones, but increased precipitation is also seen over parts of the subsidence zones in the North and South Pacific and other regions, especially for the subsidence zone defined by $\omega \ge 0$ Pa/s (Fig. 9). As a result, the mean precipitation averaged over the subsidence zones for the last 50 years increases in most of the experiments (Fig. 10d), in contrast to the decreased precipitation over the subtropical dry zones (Fig. 7d). However, when the subsidence zone is defined by $\omega > 0.01$ Pa/s, their changes (Fig. 10e-h) are more comparable to those of the subtropical dry zones (Fig. 7a–d), including decreased precipitation in the three CESM1 simulations. This seems to suggest that precipitation over areas within current climatological ω between 0 and 0.01 Pa/s may



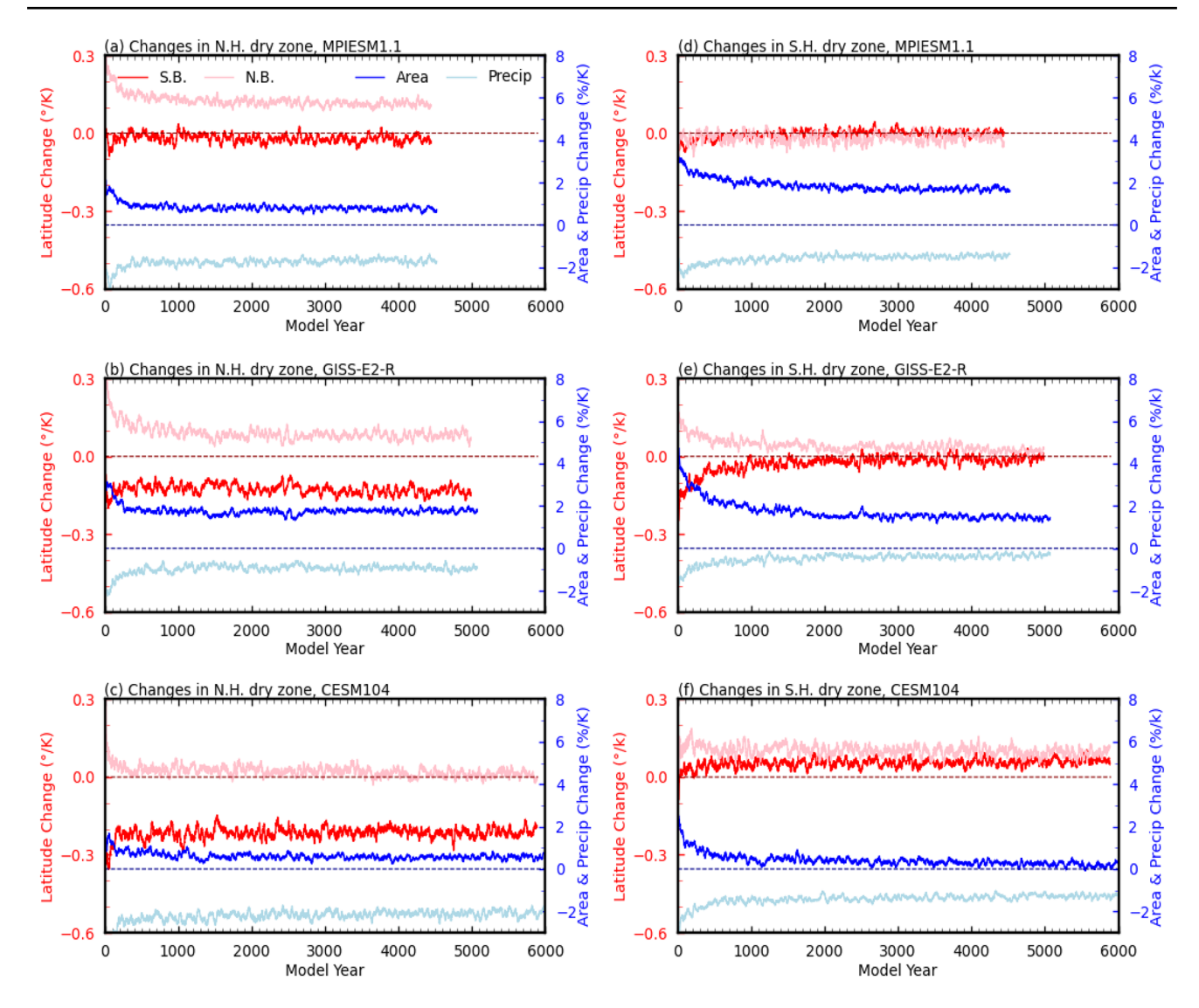


Fig. 6 Time series of the normalized 31-year moving averaged changes in subtropical dry-zone's southern boundary (S.B.) and northern boundary (N.B.) (in degrees latitude per 1 K global warming, left y-axis), dry-zone area and dry-zone mean precipitation (% change per 1 K global warming, right y-axis) in the Northern Hemisphere (left panels) and Southern Hemisphere (right panels) from the multi-millennial abrupt 4×CO₂ experiments using **a**, **d** MPI-

ESM-1.1, **b**, **e** GISS-E2-R, and **c**, **f** CESM1.0.4. The red and blue dot lines indicate the zero lines for the red curves (left y-axis) and blue curves (right y-axis), respectively. All the changes are relative to the PiControl run climatology. A positive latitude change means a poleward shift of N.H. dry zone boundaries and an equatorward shift of S.H. dry zone, vice versa for the negative change

increase due to the contribution (generally wetting effect) of increased water vapor (the 3^{rd} and 4^{th} terms on the right side of Eq. 1) that may exceed the small drying effect caused by the weak subsidence (the 1st and 2nd terms on the right side of Eq. 1). Further examination revealed that the difference between the wetting effect of increased water vapor and drying effect caused by the weaker subsidence is positive over the regions within ω between 0 and 0.01 Pa/s, with the value of both (P3-(P1+P2)) and (E-(P1+P2)) being positive (about $0.01 \sim 0.04$ mm/day and $0.17 \sim 0.2$ mm/day per 1 K global warming from the CESM simulations for both the N.H. and S.H.). Thus, future subtropical precipitation

change will be influenced by not only the drying effect of the descending motion but also the wetting effect from increased water vapor under warmer temperatures, with the latter playing a dominant role over the weak subsidence areas. Even with the $\omega \geq 0.01$ Pa/s threshold, the CMIP6 extended SSP5-8.5 simulations still show different results between Figs. 7a–d and 10e–h likely in part due to their transient nature and short length of the CMIP6 simulations, as well as different matches of our dry zones with the ω -based subsidence zones in these models.

Based on these model results, we conclude that the subtropical dry zones would expand equatorward, and also



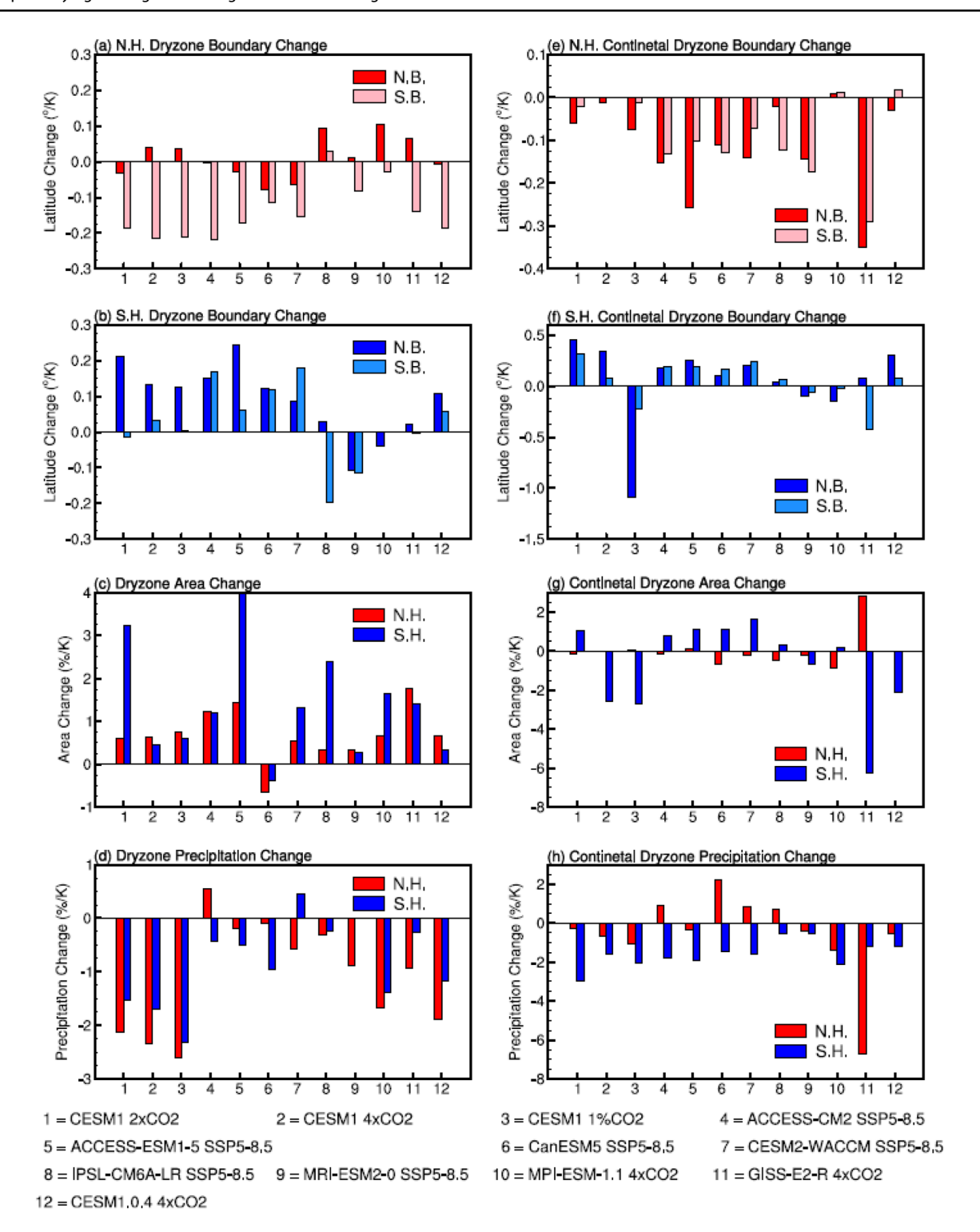


Fig. 7 Normalized changes in the subtropical dry-zone's boundary (**a**, **b**), area (**c**) and mean precipitation (**d**) averaged over the last 50 years under anthropogenic warming for all the experiments examined in this study: the CESM1 experiments, SSP5-8.5 simulations from six CMIP6 models, and three multi-millennial $4 \times \text{CO}_2$ simulations. A positive latitude change indicates a poleward shift of N.H. dry zone boundaries and an equatorward shift of S.H. dry zone, vice versa for

the negative change. All the changes are significant at the 5% level based on Student's *t*-test. The changes are relative to the PiControl climatology (for the CESM1 and multi-millennial simulations) or 1900–1999 mean (for SSP5-8.5 runs). **e**-**h** same as **a**-**d**, but for subtropical dry-zone over land only, whereas **a**-**d** include both land and ocean of the dry zones



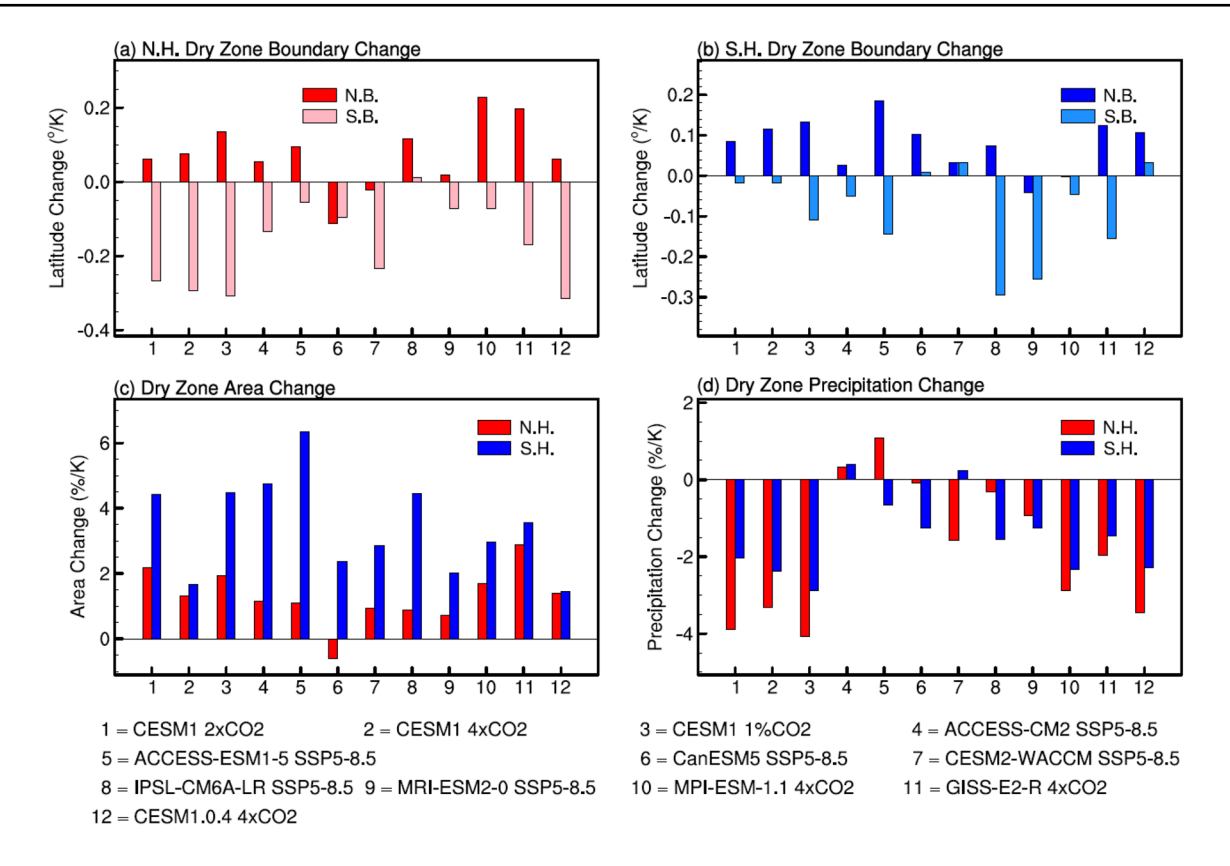


Fig. 8 Same as Fig. 7a-d, but averaged over the transient period of 51-100 years

poleward and westward in some models, while the dryzone mean precipitation would decrease under increased GHGs. Further, the expansion of the subtropical dry zones and its precipitation decrease are not temporary but permanent features of the GHG-induced climate change that are fairly steady and persist for thousands of years after a CO_2 increase. Mean precipitation over the subtropical subsidence zones with $\omega \ge 0$ Pa/s generally increases due to increased precipitation over the areas with weak subsidence, where the wetting effect of increased water vapor exceeds the drying effect of the subsidence.

4 Possible mechanisms for the subtropical dry-zone changes

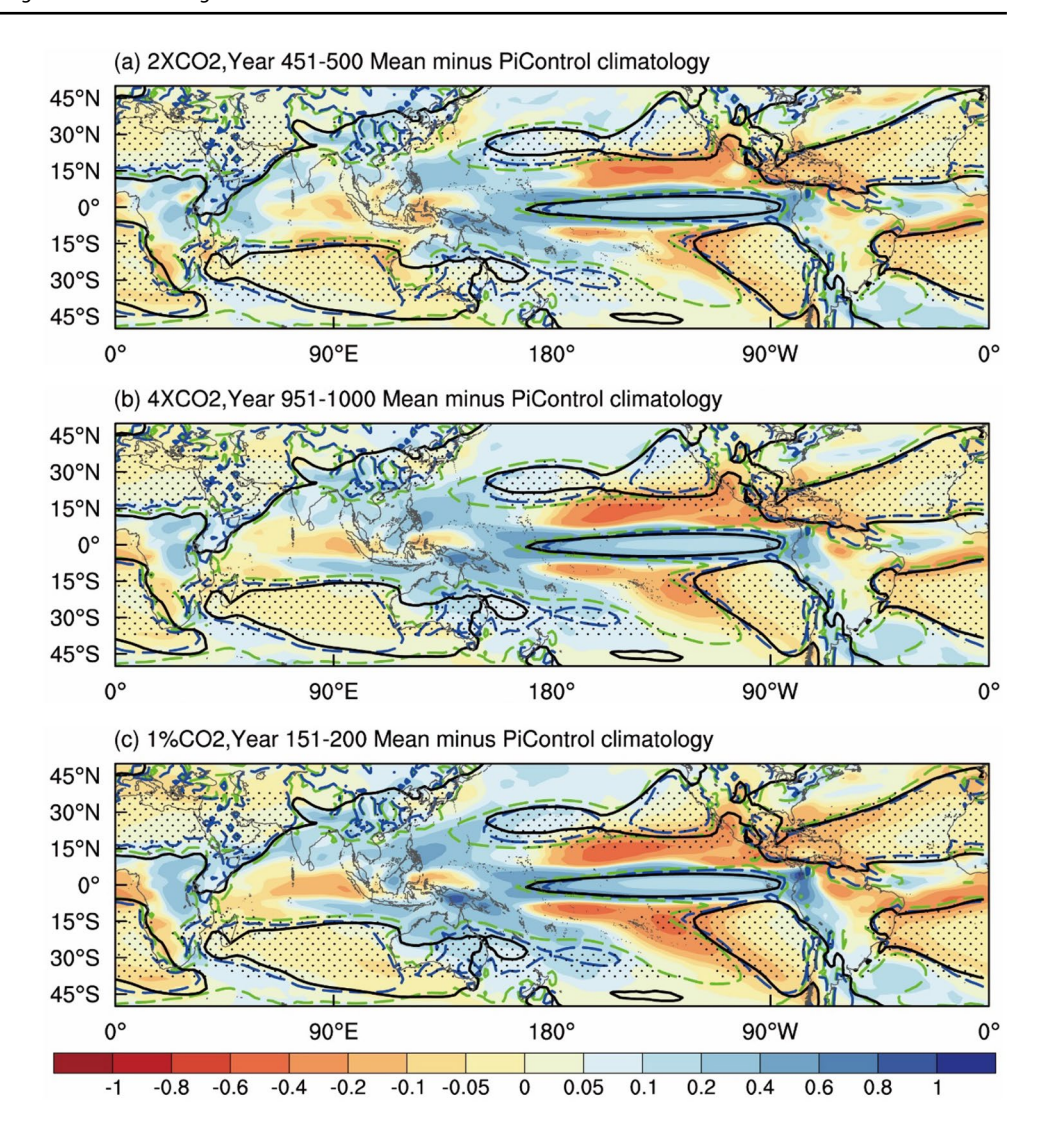
The meridional SST gradient (MTG) influences the strength of the Hadley circulation (Williamson et al. 2013; Seo et al. 2014), and hence the position and intensity of its descending subtropical branch (Sniderman et al. 2019). In their CESM1 $4\times CO_2$ experiment (at a lower resolution than ours), Burls and Fedorov (2017) have also attributed the subtropical drying partly to the meridional SST gradient change via the Hadley circulation. Since the tropical-subtropical SST gradient may affect the Hadley circulation and therefore the

subsidence and precipitation in the subtropics, in this study we firstly examine the relationships among the meridional SST gradient, subtropical precipitation (P) and subtropical pressure velocity (ω). Our results indicate that their relationships are more robust and consistent when averaged over 0° –360° longitudes than the case when averaged only over the subtropical dry zones. This may be because the subtropical subsidence and precipitation can be influenced by the MTG outside the longitudes of the subtropical dry zones, as the corresponding tropical and subtropical parts of the Hadley circulation may be located at different longitudes (e.g., connected by the trade winds). For this reason, here we focus on the relationships among the zonal-mean of these three variables.

Figure 11 shows that on an annual basis, in the three CESM1 experiments a strong MTG is associated with strong subtropical descending motion and reduced subtropical-mean precipitation in both hemispheres, although the relationship is stronger in the S.H. Similar relationships are seen in the SSP5-8.5 simulations from the six CMIP6 models and three long abrupt $4 \times \text{CO}_2$ simulations (scatter plots not shown). Figure 12 summarizes the correlation coefficients among the MTG, subtropical-mean precipitation and subtropical-mean vertical velocity from all the experiments analyzed here. Except the weak relationships in a few cases,



Fig. 9 Normalized annual-mean precipitation change (in mm/day per 1 K global warming, shading, relative to PiControl climatology) from CESM1 a 2×CO₂ (for years 151–200), **b** $4 \times CO_2$ (for years 451–500) and c 1% CO₂ (for years 951-1000). Also shown are isolines of 2.5 mm/ day annual-mean precipitation (black solid), as well as 0 Pa/s pressure velocity (green dashed) and 0.1 Pa/s pressure velocity (blue dashed) at the 500 hPa level. The dots indicate the subtropical dry zone with downward motion within 10°S-40°S and 10°N-40°N in each experiment for the stated time period, which may differ from the PiControl run (outlined by the blue dashed contour)



most of the simulations consistently show significant correlations among the three variables, with a strong MTG leading to increased subtropical subsidence and decreased subtropical precipitation. Associated with the strong MTG and strong subtropical subsidence, the subtropical dry-zone area also generally increases in the three CESM1 experiments (Fig. 13, except panel c) and other model simulations (except for the CESM2-WACCM model, Fig. 14). Overall, most simulations show that a strong MTG is associated with strengthened subtropical subsidence, reduced subtropical precipitation and increased subtropical dry-zone area.

Drying is a balancing act of various processes and each term in the moisture budget equation can play a role in the changes of subtropical dry-zone precipitation. Here, we focus on the persistent increase of water vapor under rising temperatures that can cause persistent drying through subsidence due to increased vertical gradient of water vapor (P1 in Eq. 1). Both increased vertical gradient of water vapor (P1) and increased descending motion (P2) over the

subtropical dry zones can lead to a precipitation decrease there (Fig. 16). In the CESM1 experiments, the change pattern of P1 (Fig. 15a-c) broadly resembles that of precipitation (Fig. 1c-e) over the subtropical dry zones, especially over the subtropical North Pacific and North Atlantic Ocean. In contrast, P2 reduces precipitation mainly around the equatorward boundary of the subtropical dry zones in the $2 \times CO_2$ and $1\% CO_2$ runs (Fig. 15d, f), but it also extends to most of the subtropics in the $4 \times CO_2$ run (Fig. 15e). We further examined the conventional thermodynamic term P3 and local evaporation term E, and found that the spatial pattern of P3 is similar to that of P1 + P2 over the subtropical dry zones (figure not shown), but with much smaller values. Meanwhile, local evaporation change (E) is positive with large values (figure not shown). Figure 16 shows that P1 leads to precipitation decreases in all the experiments, representing the drying effect due to increased vertical gradients of water vapor content. P2 decreases in the three CESM1 runs and three CMIP6 simulations (as ACCESS-CM2,



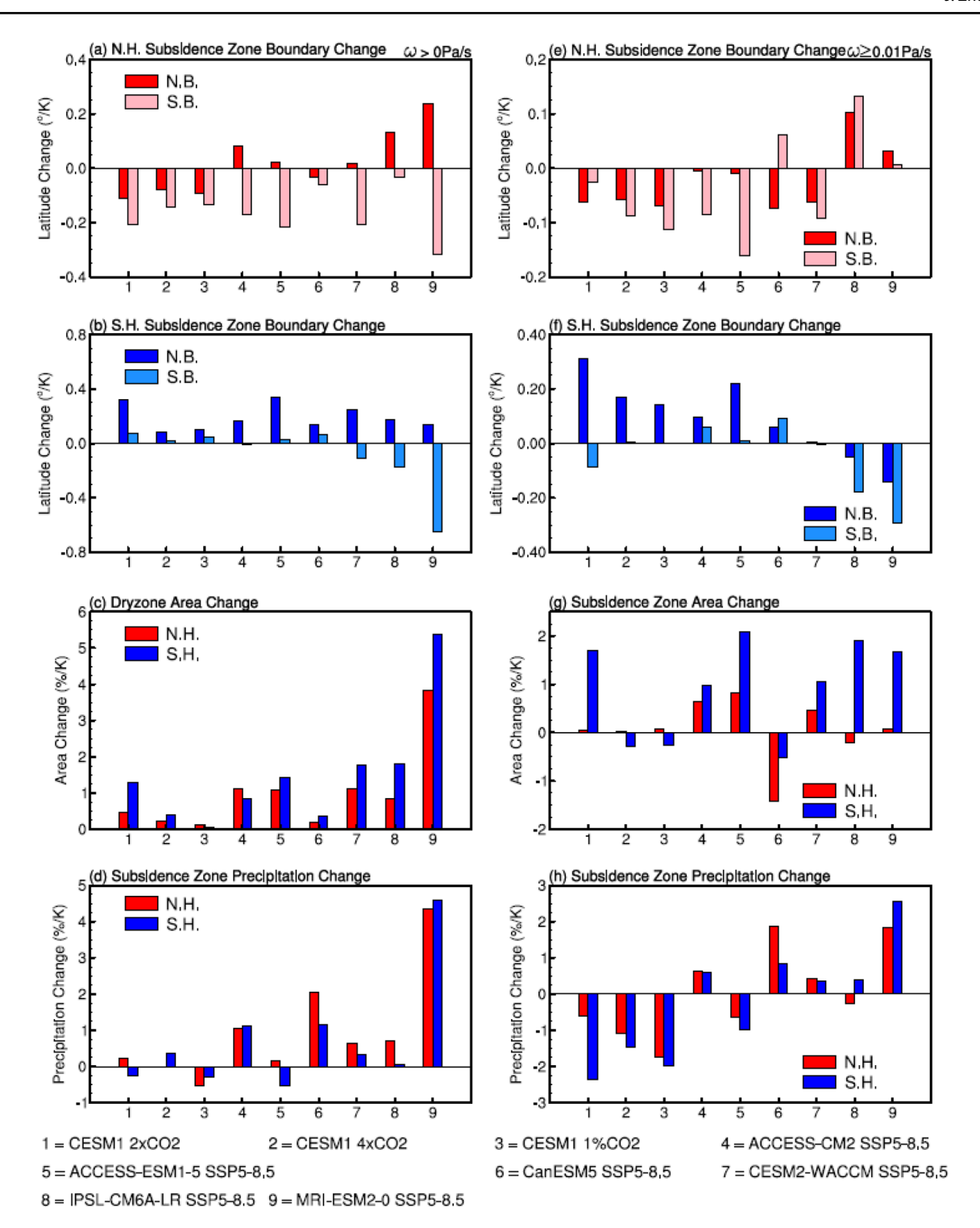


Fig. 10 Normalized changes in the subtropical subsidence zone's (defined by omega>0 Pa/s, left panels, omega≥0.01 Pa/s, right panels) boundary (a-b, e-f), area (c, g) and mean precipitation (d, h) averaged over the last 50 years under anthropogenic warming for the CESM1 experiments and SSP5-8.5 simulations from six CMIP6 models. A positive latitude change means a poleward shift of N.H.

dry zone boundaries and an equatorward shift of S.H. dry zone, vice versa for the negative change. All the changes are significant at the 5% level based on Student's t-test. The changes are relative to the PiControl climatology (for the CESM1 experiments) or 1900-1999 mean (for SSP5-8.5 runs)



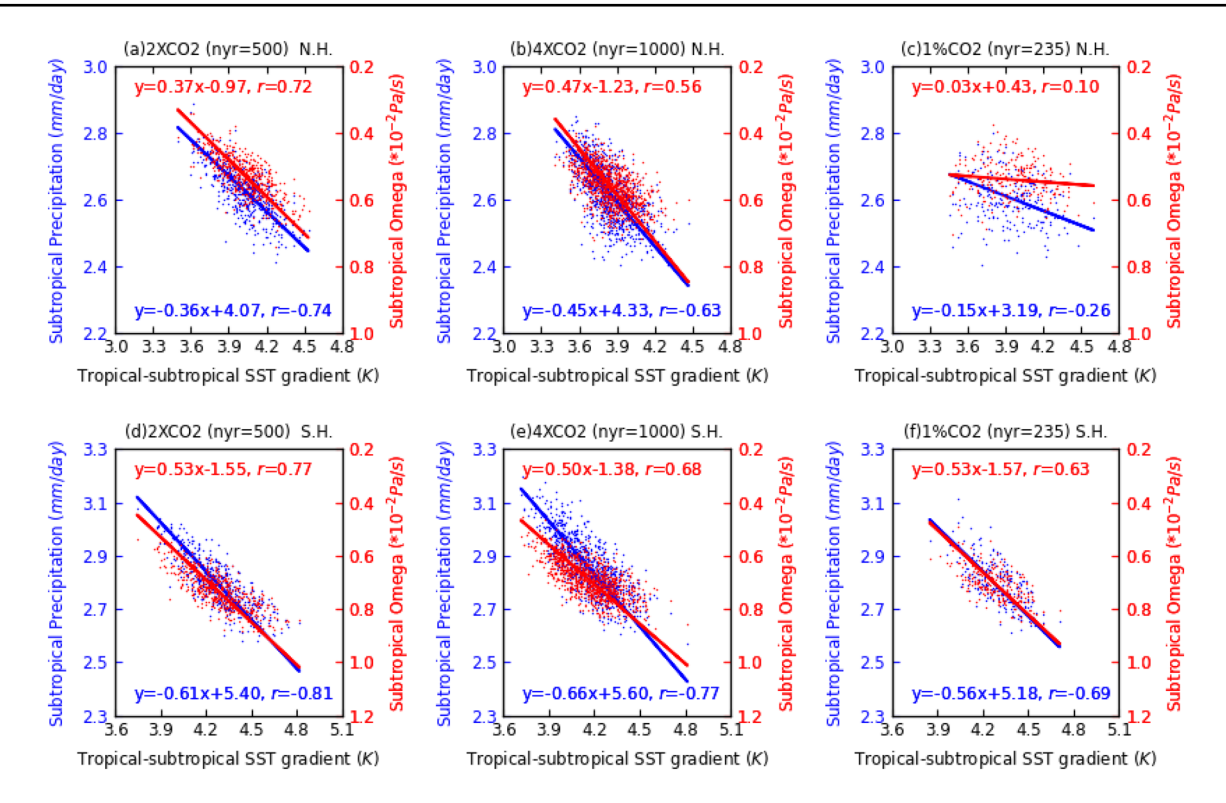


Fig. 11 Scatter plots of the annual zonal-mean meridional SST gradient (MTG, unit: K) vs. annual subtropical-mean precipitation (mm/day, blue dots and line, left y-axis), or vs. subtropical-mean pressure vertical velocity (ω , in 10^{-2} Pa/s, red dots and line, right y-axis, positive downward) in the CESM1 **a**, **d** $2 \times \text{CO}_2$, **b**, **e** $4 \times \text{CO}_2$ and **c**, **f** 1%

 ${\rm CO_2}$ experiments in the **a-c** Northern Hemisphere and **d**, **e** Southern Hemisphere. The regression line and equation (in the same color as the dots, each dot is for one year) and the number of simulation years (nyr) are also shown

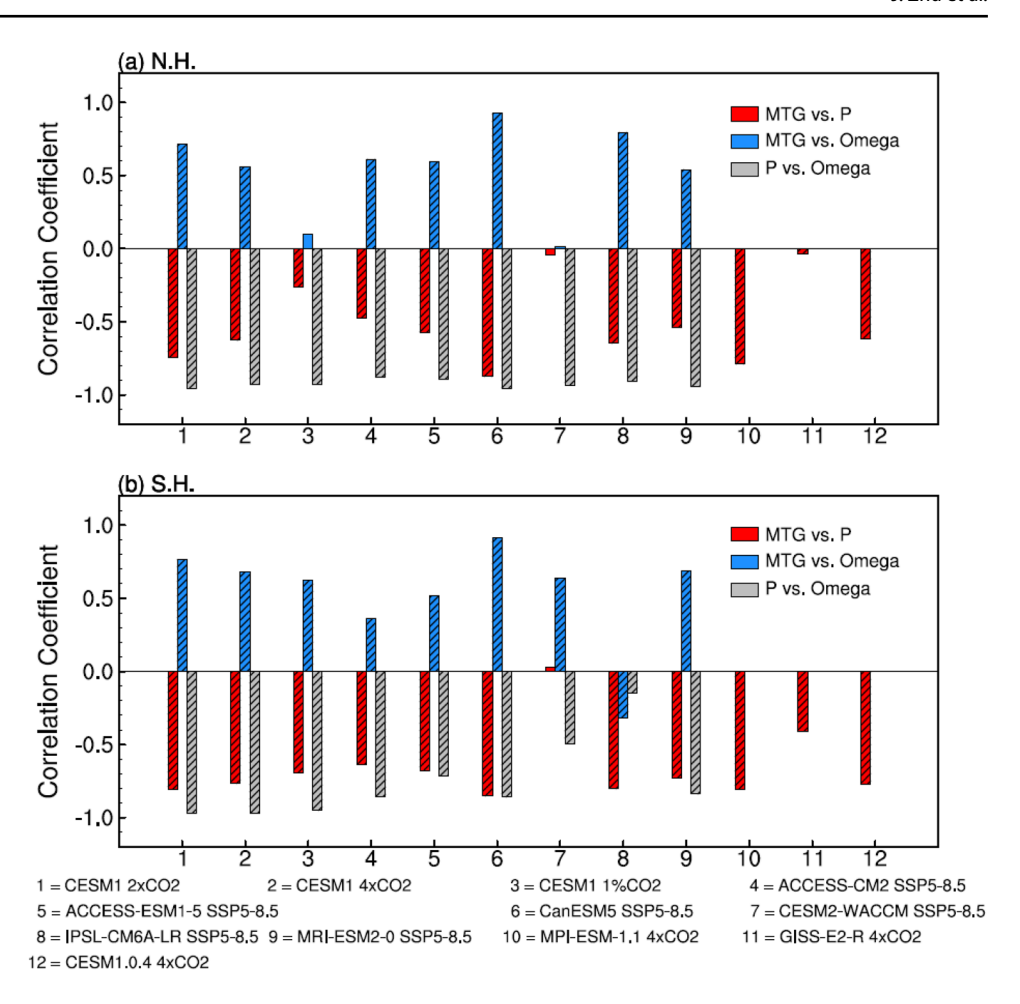
ACCESS-ESM1-5 and CESM2-WACCM2), but increases slightly or changes little in the other three CMIP6 models. P3 is very small (near zero) and negative in most experiments over the whole dry-zone regions, which differs from that over the regions with ω between 0 and 0.01 Pa/s. These changes indicate that the drying effect is mainly due to P1. Additionally, the sum of P1 + P2 + P3 exceeds the modelsimulated precipitation decrease in all simulations, whereas the local evaporation change (E, 4th term in Eq. 1) is positive and quite large, suggesting that the drying effect (mainly from P1) is partly offset by the wetting effect from increased local evaporation. Additionally, we notice that local evaporation also increases with rising temperatures over oceanic dry zones, but follows precipitation changes over land that show decreases in many of the simulations, especially over the Southern Hemisphere dry-zone (figures not shown). Thus, over ocean P1, P2 and P3 all contribute to the subtropical drying with P1 playing a dominant role, while increased E partially offsets the drying. Over land, drying from P1 dominates in the Northern Hemisphere dry zone, while decreased E and wetting from P2 dominate in the Southern Hemisphere dry zone. Overall, the enhanced drying from subsidence due to increased vertical gradients of water vapor (P1) would greatly reduce subtropical precipitation, with some

additional drying effect from increased descending motion (P2) in the subtropics; while increased local evaporation (E, mainly over ocean) would partly offset these drying effects (P1+P2+P3), leading to moderate decreases in subtropical precipitation.

The enhanced drying of the mid-lower troposphere by subsidence due to increased vertical gradient of water vapor (i.e., P1) has been noticed before (Chou et al. 2009; Dai et al. 2018). This enhanced drying occurs even without a change in the strength of the subsidence. This occurs because specific humidity q increases much faster in the lower troposphere than in the upper troposphere under GHG-induced warming (Fig. 17) because q, which is much larger in the lower troposphere, increases roughly by ~7%/K at all levels following the Clausius-Clapeyron equation as changes in relative humidity are small (Chen et al. 2020). This occurs in all the CESM1 simulations, over different periods, and persists to the end of the simulations (Fig. 17). The q changes depend mainly on tropospheric warming and thus are robust and permanent changes caused by the increased GHGs. In general, the q changes from the six CMIP6 simulations and our CESM1 experiments are in good agreement qualitatively. The q change is a thermodynamic response to GHG forcing that should exist in both the transient and equilibrium



Fig. 12 Correlation coefficients of annual variations between the zonal-mean MTG and subtropical-mean precipitation (blue bar) or pressure velocity (red bar) and between subtropical-mean precipitation and pressure velocity (gray bar) in the a Northern Hemisphere and b Southern Hemisphere for all the experiments analyzed here. The values significant at the 5% level based on a Student's *t*-test are marked with stripes



responses. Thus, we expect its drying effect to exist even as the system approaches a new equilibrium after increased GHGs. In addition, we further showed that increased subsidence (P2), which represents a dynamic change, would also contribute to the subtropical drying in all the CESM1 and CESM2 simulations, but not in the other models (Fig. 16).

5 Summary and discussion

In this study, we have examined and compared the subtropical drying in response to increasing GHGs over different time periods and across different forcing scenarios $(2\times CO_2, 4\times CO_2 \text{ and } 1\% CO_2)$ using long-term simulations by the CESM1, together with those from the six CMIP6 SSP5-8.5 simulations and abrupt $4\times CO_2$ multimillennium simulations from three coupled models. We first defined the subtropical dry zones within 10° – 40° S and 10° – 40° N using grid boxes whose annual-mean precipitation is below 2.5 mm/day, and then examined the changes in subtropical dry-zone boundaries, area and mean precipitation under increasing GHGs. Most of the model simulations consistently show a substantial equatorward shift

of the southern boundary and a slight poleward shift of the northern boundary in the Northern Hemisphere (N.H.) subtropical dry zones after the initial transient period of ~ 150 years. These changes lead to an increase in the N.H. dry-zone area. In the Southern Hemisphere (S.H.), although changes differ among different simulations, most of them show an equatorward shift for both the northern and southern boundaries of the S.H. subtropical dry zones after the initial transient period, and an increase in dryzone area mainly due to a westward expansion of the dry zone in the South Pacific. The dry-zone boundaries expand both equatorward and poleward during the transient period in both hemispheres, consistent with previous studies (Scheff and Frierson 2012b; Lu et al. 2007; Gastineau et al. 2008; Hu et al. 2013; Tao et al. 2016). Also consistent with previous studies, the mean precipitation over the subtropical dry zones decreases. Furthermore, the dryzone precipitation decreases and other associated changes exist over different periods, under different forcing scenarios, and persist into equilibrium states. Our results from various experiments using different models under different forcing scenarios suggest that these changes are likely permanent, rather than temporary, response to increasing



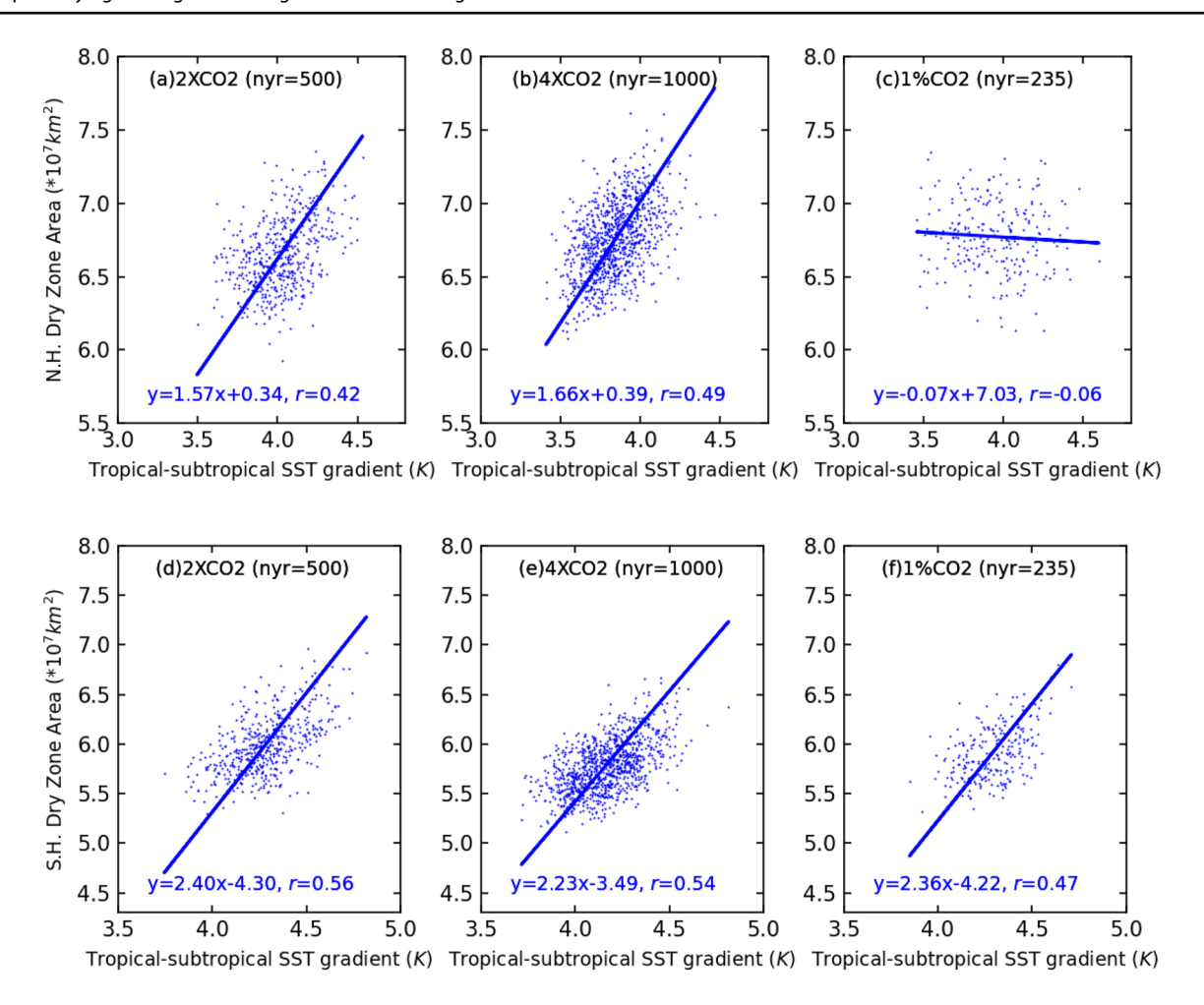
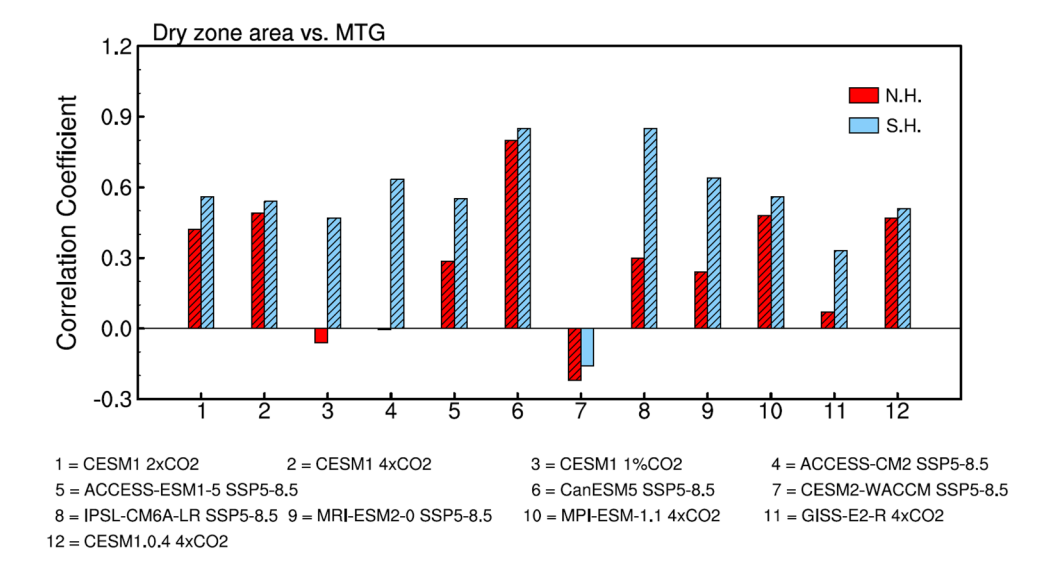


Fig. 13 Scatter plots of the annual zonal-mean MTG vs. annual subtropical dry-zone area (10^7 km^2) in the CESM1 **a**, **d** $2 \times \text{CO}_2$, **b**, **e** $4 \times \text{CO}_2$ and **c**, **f** 1% CO₂ experiments in the **a–c** Northern Hemi-

sphere and $\boldsymbol{d},\,\boldsymbol{e}$ Southern Hemisphere. The regression line and equation and the number of simulation years (nyr) are also shown

Fig. 14 Correlation coefficients of interannual variations between the zonal-mean MTG and subtropical dry-zone area for all the experiments analyzed here. The values significant at the 5% level based on a Student's *t*-test are marked with stripes





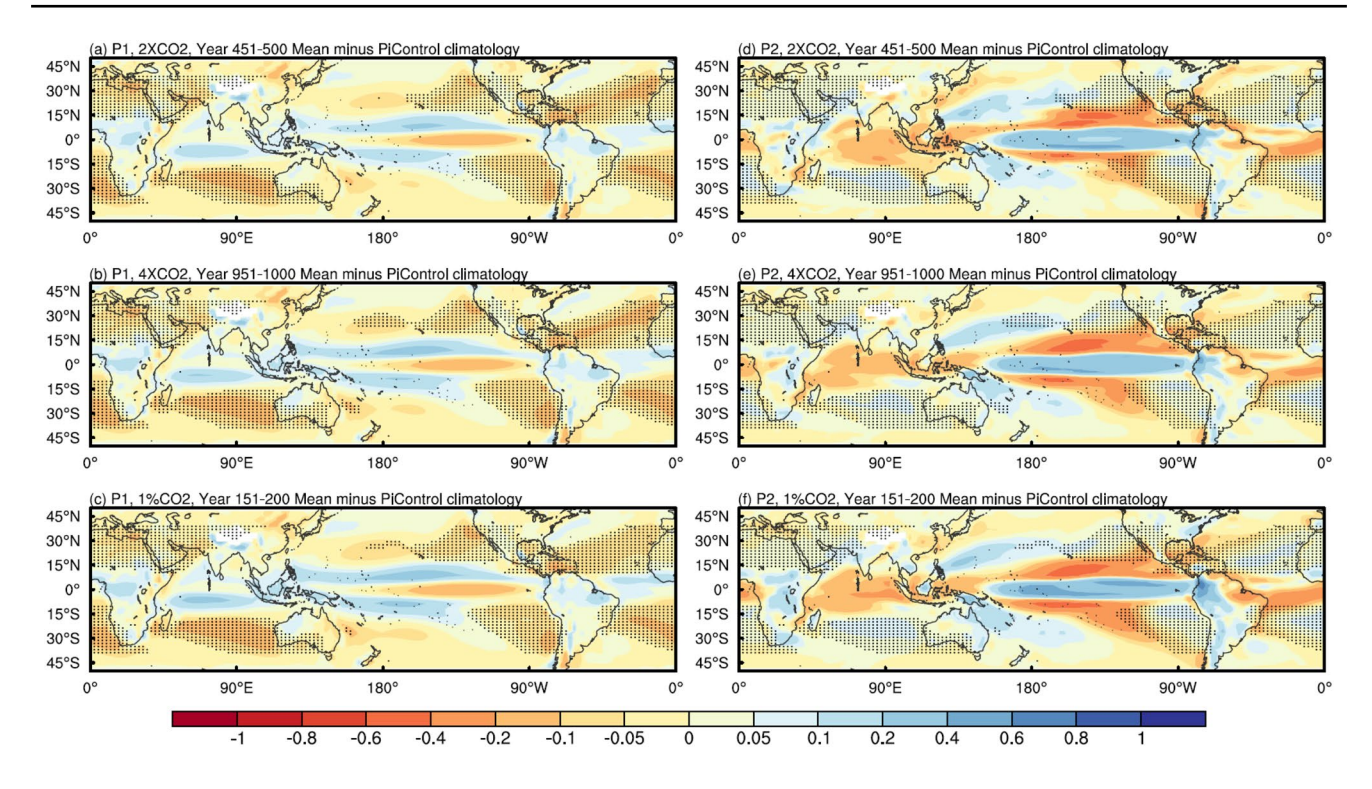


Fig. 15 Normalized (a–c) P1 $(-\langle \overline{\omega} \partial_{\rho} q' \rangle)$ and (d-f) P2 $(-\langle \omega' \partial_{\rho} \overline{q} \rangle)$ changes (mm/day per 1 K global warming) from CESM1 a, b 1% CO₂ (for years 151–200), c, d 2×CO₂ (for years 451–500) and e, f

 $4\times CO_2$ (for years 951–1000) simulations. The dotted areas indicate the subtropical dry zone with annual-mean precipitation below 2.5 mm/day within $10^{\circ} S-40^{\circ} S$ and $10^{\circ} N-40^{\circ} N$ in each experiment for the stated time period

GHGs. We also examined the zonal-mean precipitation averaged over the entire 25°S-35°S zone as in Sniderman et al. (2019) and found either little change or some increases toward the end of the long simulations (figure not shown); however, the increased precipitation comes mainly from relatively wet areas over the oceans and South America within 25°S-35°S (Figs. 2, 3), rather than from the dry zone areas. Thus, the zonal-mean precipitation change averaged over 25°S-35°S is not representative of that over the S.H. subtropical dry zone, which shows consistent drying in different long simulations.

These subtropical dry-zone changes, including the decreased precipitation, are qualitatively consistent with those for the subtropical subsidence zones outlined by vertical velocity $\omega \geq 0.01$ Pa/s instead of $\omega \geq 0$ Pa/s in the CESM1 simulations. In particular, mean precipitation averaged over subsidence zones based on $\omega \geq 0$ Pa/s would increase mainly because the wetting effect from increased water vapor (through moisture convergence and local evaporation) would exceed the drying effects from increased vertical gradients of water vapor and increased downward motion over areas with weak subsidence ($0 < \omega < 0.01$ Pa/s). Thus, precipitation and other changes for subtropical subsidence zones defined using $\omega \geq 0$ Pa/s (e.g., Chou et al. 2009) may not be comparable

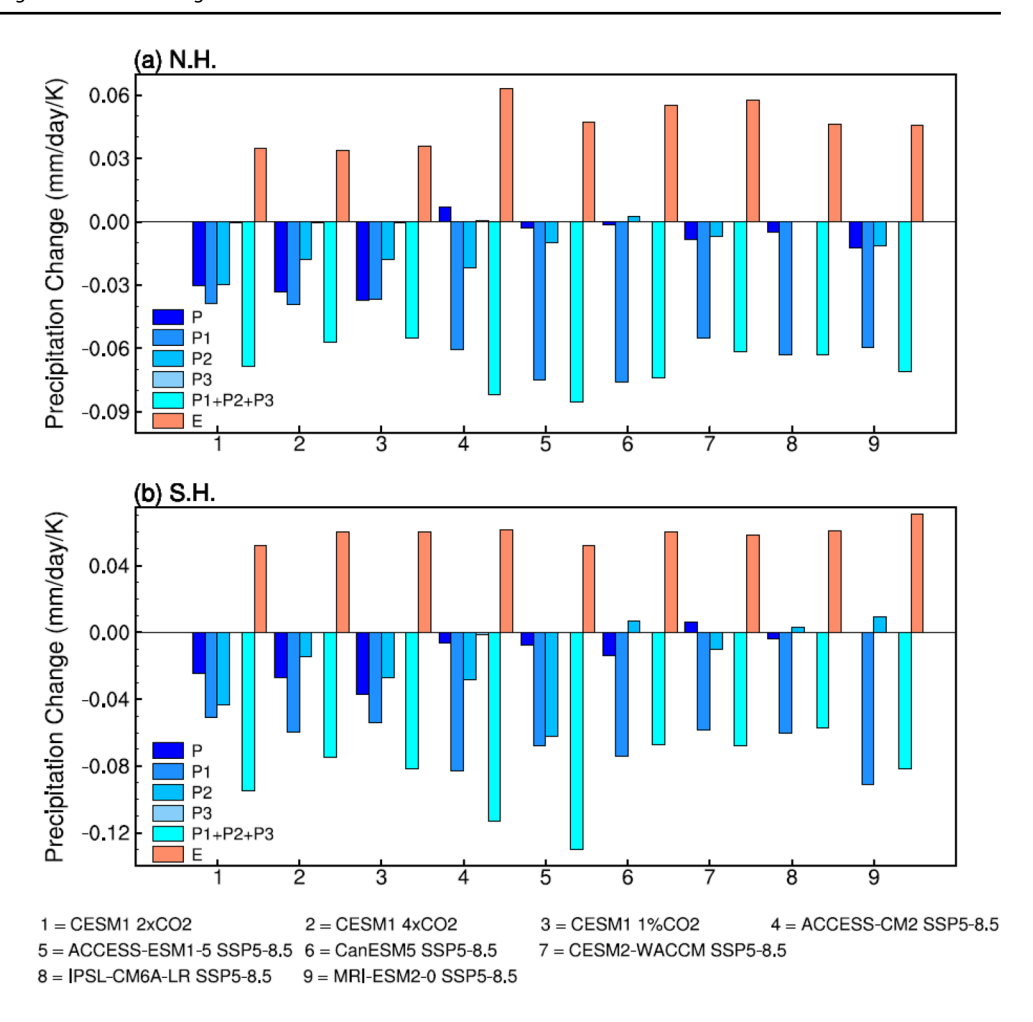
with those for subtropical dry zones defined using a precipitation-based threshold.

In most of the simulations, a strong zonal-mean equatorsubtropical (0°-10°N/S minus 10°-40°N/S) SST gradient (MTG) is usually associated with enhanced subtropical subsidence, increased subtropical dry-zone area, and decreased subtropical precipitation. This mechanism is in addition to the enhanced drying of the lower troposphere by subsidence due to increased vertical gradient of water vapor (P1 in Eq. 1) in the subtropics as noticed previously (Chou et al. 2009; Dai et al. 2018). However, the long-term changes in zonal-mean MTG and subtropical ω differ among the model simulations (figures not shown), and they tend to be small and exhibit weak relationships between them, in contrast to the robust relationships revealed by their interannual variations. Thus, we cannot conclude that GHG-induced warming would increase or decrease MTG, contributing to increased or weakened subsidence in the subtropics.

Our calculations indicate that the drying results from the increased vertical gradient of water vapor dominates, with some additional drying from increased downward motion. The drying is partly offset by the wetting effect from increased local evaporation (E), leading to only moderate decreases in subtropical precipitation. The water vapor vertical gradient change (P1) mainly depends on tropospheric



Fig. 16 Normalized changes (in mm/day per 1 K global warming) in the subtropical dry-zone precipitation (P), $-\langle \overline{\omega} \partial_n q' \rangle$ (P1), $-\langle \omega' \partial_n \overline{q} \rangle (P2)$, $\vec{V} \cdot \nabla q'$ (P3, with control run winds), E', and the sum of them averaged over the last 50 years under anthropogenic warming for the CESM1 experiments and SSP5-8.5 simulations from six CMIP6 models. The changes are relative to the PiControl climatology (for the CESM1) or 1900-1999 mean (for CMIP6 runs)



warming and thus should persist into the new equilibrium state after a GHG increase. This implies that the subtropical drying is not just a temporary phenomenon of the transient climate response but would persist into the new equilibrium state.

The changes in downward motion over the subtropics seem to be unrelated to the diverse changes in low-latitude SST gradients among the simulations, which are also inconsistent with a weakened Hadley circulation under GHG-induced warming (Dai et al. 2001; Held and Soden 2006; Vecchi and Soden 2007; Chadwick et al. 2013; Rosa and Collins 2013). As noticed by Dai et al. (2001), the weakening of the time-mean Hadley circulation is likely related to the increased tropical stability associated with vertical cloudiness changes (Wang and Rossow 1998), rather than the SST gradient changes. The reduction in the number of convective events due to the imbalance in the change rates of surface evaporation and precipitation intensity would also lead to a decrease in the time-mean vertical motion in the deep tropics (Dai et al. 2020). However, it is unclear how a

weakened Hadley circulation would lead to stronger subsidence in the subtropics.

Consistent with Huang et al. (2020), our results suggest that the warming patterns and the associated precipitation change patterns over the subtropics during the twenty-first century are likely to be similar to those when the system reaches a new equilibrium, except for the slightly different expansions of the dry-zone boundaries during the transient period. Thus, the difference between the transient and equilibrium change patterns is likely to be small and cannot explain the wetter subtropics during the early-middle Pliocene (Burls and Fedorov 2017). To overcome the drying mechanisms discussed here, other processes, such as a weakened meridional temperature gradient over the low latitudes and thus weakened subtropical subsidence, would need to play a much bigger role during the early-middle Pliocene. However, such changes are absent in model simulations examined here, even as the system approaches a new equilibrium. Furthermore, this study investigates the change of subtropical dry zones only under GHG-induced



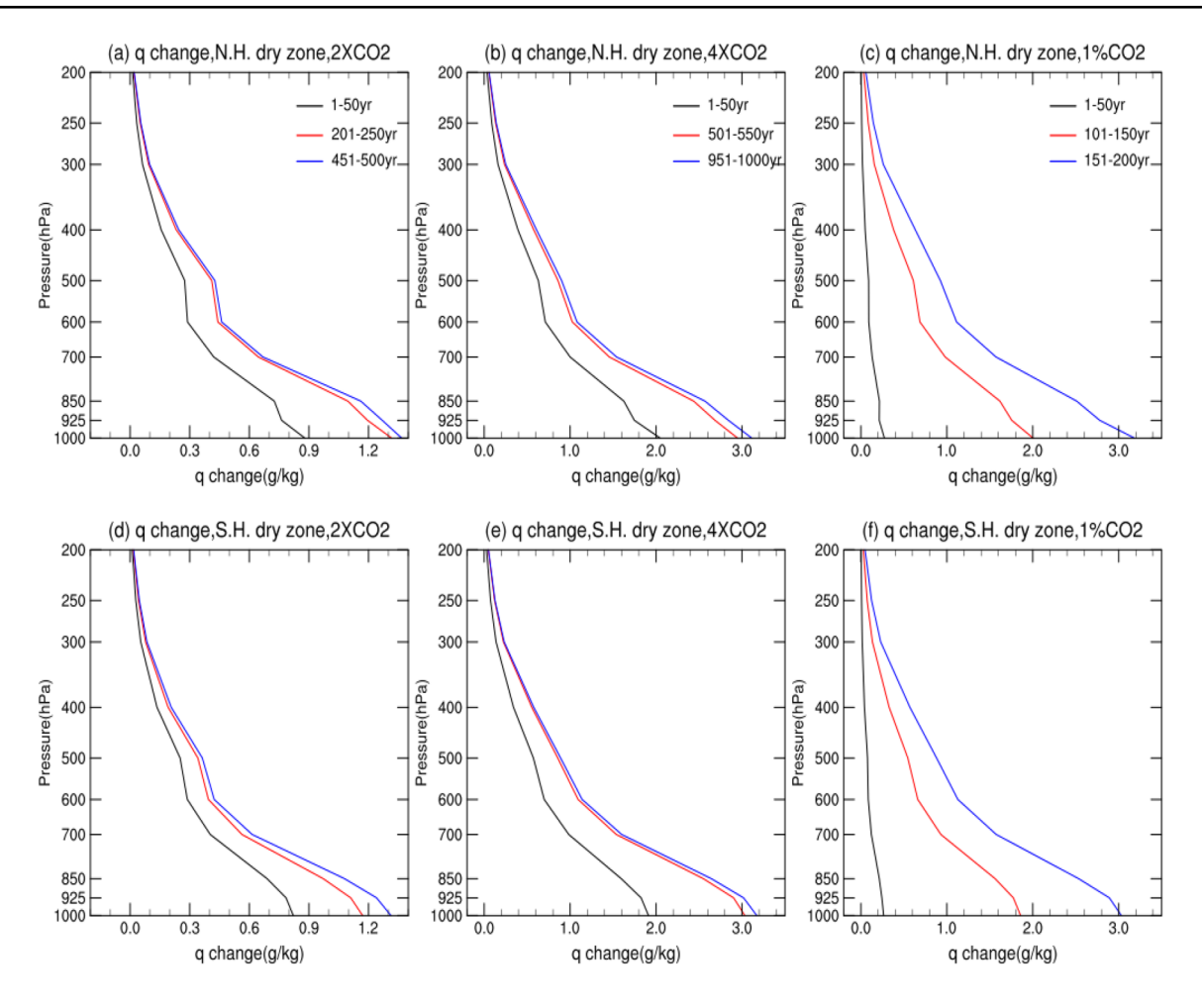


Fig. 17 Vertical profiles of zonal-mean specific humidity changes averaged over the subtropical dry zone in the N.H. (**a–c**) and S.H. (**d–f**) for different periods (unit: g/kg) relative to the PiControl cli-

matology in the CESM1 experiments from the (**a**, **d**) $2 \times CO_2$, (**b**, **e**) $4 \times CO_2$, and (**c**, **f**) 1% CO_2 experiments

warming. Changes in response to other forcing agents (e.g., aerosols and ozone) still need to be investigated.

Acknowledgements This study was jointly sponsored by the National Key Research and Development Program of China (Grant No. 2022YFC3202801) and National Natural Science Foundation of China (Grant No. 42075020), the Research Funds for the Frontiers Science Center for Critical Earth Material Cycling and the Fundamental Research Funds for the Central Universities (0209-14380104). Dai acknowledges the funding support from the U.S. National Science Foundation (Award Nos. AGS-2015780 and OISE-1743738).

Author contributions All authors contributed to the study conception, design, and development. Material preparation, data collection, and analysis were performed by all authors. The first draft of the manuscript was written by JZ, DH and AD and all authors commented on previous versions of the manuscript.

Funding This study was jointly sponsored by the National Key Research and Development Program of China (Grant No. 2022YFC3202801) and National Natural Science Foundation of China (Grant No. 42075020), the Research Funds for the Frontiers Science Center for Critical Earth Material Cycling and the Fundamental

Research Funds for the Central Universities (0209-14380104). Dai acknowledges the funding support from the U.S. National Science Foundation (Award Nos. AGS-2015780 and OISE-1743738).

Data availability The abrupt 4×CO₂ multi-millennium simulations from three coupled models (MPI-ESM-1.1, GISS-E2-R, and CESM1.0.4) obtained from https://data.iac.ethz.ch/longrunmip/; The CMIP6 model data used in this study can beaccessed at the ESGF portal (https://esgf-node.llnl.gov/projects/esgf-llnl/); The long simulations with the CESM1 forthree experiments for this research are included in Huang et al. (2020).

Declarations

Conflict of interest The authors declare no competing interests.

References

Adler RF, Sapiano MRP, Huffman GJ et al (2018) The Global Precipitation Climatology Project (GPCP) monthly analysis (New



- Version 2.3) and a review of 2017 global precipitation. Atmosphere (Basel). https://doi.org/10.3390/atmos9040138
- Burls NJ, Fedorov AV (2017) Wetter subtropics in a warmer world: Contrasting past and future hydrological cycles. Proc Natl Acad Sci. https://doi.org/10.1073/pnas.1703421114
- Byrne MP, Pendergrass AG, Rapp AD, Wodzicki KR (2018) Response of the intertropical convergence zone to climate change: location, width and strength precipitation climatology. Curr Clim Chang Rep 4:355–370
- Chadwick R, Boutle I, Martin G (2013) Spatial patterns of precipitation change in CMIP5: why the rich do not get richer in the tropics. J Clim 26:3803–3822. https://doi.org/10.1175/JCLI-D-12-00543.1
- Chen J, Dai A, Zhang Y, Rasmussen KL (2020) Changes in the convective potential available energy and convective inhibition under global warming. J Climate 33:2025–2050. https://doi.org/10.1175/JCLI-D-19-0461.1
- Chou C, Neelin JD, Chen CA, Tu JY (2009) Evaluating the "rich-get-richer" mechanism in tropical precipitation change under global warming. J Clim 22:1982–2005. https://doi.org/10.1175/2008JCLI2471.1
- Dai A, Bloecker CE (2019) Impacts of internal variability on temperature and precipitation trends in large ensemble simulations by two climate models. Clim Dyn 52:289–306. https://doi.org/10.1007/s00382-018-4132-4
- Dai A, Fyfe JC, Xie S-PP, Dai X (2015) Decadal modulation of global surface temperature by internal climate variability. Nat Clim Chang 5:555–559. https://doi.org/10.1038/nclimate2605
- Dai A, Wigley TML, Boville BA et al (2001) Climates of the 20th and 21st centuries simulated by the NCAR climate system model. J Clim 14:485–519. https://doi.org/10.1175/1520-0442(2001)014
- Dai A, Rasmussen RM, Liu C et al (2020) A new mechanism for warm-season precipitation response to global warming based on convection-permitting simulations. Clim Dyn 55:343–368. https://doi.org/10.1007/s00382-017-3787-6
- Dai A, Zhao T, Chen J (2018) Climate change and drought: a precipitation and evaporation perspective. Curr Clim Chang Rep 4:301–312. https://doi.org/10.1007/s40641-018-0101-6
- Davis N, Birner T (2017) On the discrepancies in tropical belt expansion between reanalyses and climate models and among tropical belt width metrics. J Clim 30:1211–1231. https://doi.org/10.1175/JCLI-D-16-0371.1
- Delworth TL, Zeng F (2014) Regional rainfall decline in Australia attributed to anthropogenic greenhouse gases and ozone levels. Nat Geosci 7:583–587. https://doi.org/10.1038/NGEO2201
- Dong B, Dai A (2015) The influence of the interdecadal Pacific oscillation on temperature and precipitation over the Globe. Clim Dyn. https://doi.org/10.1007/s00382-015-2500-x
- Eyring V, Bony S, Meehl GA et al (2016) Overview of the Coupled Model Intercomparison Project Phase 6 (CMIP6) experimental design and organization. Geosci Model Dev 9:1937–1958. https://doi.org/10.5194/gmd-9-1937-2016
- Fedorov AV, Brierley CM, Lawrence KT et al (2013) Patterns and mechanisms of early Pliocene warmth. Nature 496:43–49. https://doi.org/10.1038/nature12003
- Fedorov AV, Burls NJ, Lawrence KT, Peterson LC (2015) Tightly linked zonal and meridional sea surface temperature gradients over the past five million years. Nat Geosci 8:975–980. https://doi.org/10.1038/ngeo2577
- Feng S, Fu Q (2013) Expansion of global drylands under a warming climate. Atmos Chem Phys 13:10081–10094. https://doi.org/10.5194/acp-13-10081-2013

- Fu Q, Lin P (2011) Poleward shift of subtropical jets inferred from satellite-observed lower-stratospheric temperatures. J Clim 24:5597–5603. https://doi.org/10.1175/JCLI-D-11-00027.1
- Gastineau G, Le Treut H, Li L (2008) Hadley circulation changes under global warming conditions indicated by coupled climate models. Tellus Ser A Dyn Meteorol Oceanogr 60:863–884. https://doi.org/10.1111/j.1600-0870.2008.00344.x
- He J, Soden BJ (2016) A re-examination of the projected subtropical precipitation decline. Nat Clim Chang 7:53–57. https://doi.org/10.1038/NCLIMATE3157
- Held IM, Soden BJ (2006) Robust responses of the hydrological cycle to global warming. J Clim 19:5686–5699. https://doi.org/10.1175/JCLI3990.1
- Hu Y, Fu Q (2007) Observed poleward expansion of the Hadley circulation since 1979. Atmos Chem Phys Discuss 7:9367–9384. https://doi.org/10.5194/acpd-7-9367-2007
- Hu Y, Tao L, Liu J (2013) Poleward expansion of the Hadley circulation in CMIP5 simulations. Adv Atmos Sci 30:790–795. https://doi.org/10.1007/s00376-012-2187-4
- Huang J, Li Y, Fu C et al (2017a) Dryland climate change: recent progress and challenges. Rev Geophys 55:719–778. https://doi. org/10.1002/2016RG000550
- Huang J, Yu H, Dai A et al (2017b) Drylands face potential threat under 2 °c global warming target. Nat Clim Chang 7:417–422. https://doi.org/10.1038/nclimate3275
- Huang D, Dai A, Zhu J (2020) Are the transient and equilibrium climate change patterns similar in response to increased CO₂? J Clim 33:8003–8023. https://doi.org/10.1175/JCLI-D-19-0749.1
- Huang D, Liu A, Zheng Y, Zhu J (2022) Inter-model spread of the simulated East Asian Summer Monsoon Rainfall and the associated atmospheric circulations from the CMIP6 models. J Geophys Res Atmos 127:e2022JD037371. https://doi.org/10.1029/ 2022JD037371
- Hurrell JW, Holland MM, Gent PR et al (2013) The community earth system model: a framework for collaborative research. Bull Am Meteorol Soc 94:1339–1360. https://doi.org/10.1175/BAMS-D-12-00121.1
- Liu A, Huang Y, Huang D (2022) Inter-model spread of the simulated winter surface air temperature over the eurasian continent and the physical linkage to the jet streams from the CMIP6 models. J Geophys Res Atmos 127:e2022JD037172. https://doi.org/10.1029/2022JD037172
- Lu J, Vecchi G a., Reichler T (2007) Expansion of the Hadley cell under global warming. Geophys Res Lett 34:L06805. https://doi.org/10.1029/2006GL028443
- Meinshausen M, Smith SJ, Calvin K et al (2011) The RCP greenhouse gas concentrations and their extensions from 1765 to 2300. Clim Change 109:213–241. https://doi.org/10.1007/s10584-011-0156-z
- Rosa D, Collins WD (2013) A case study of subdaily simulated and observed continental convective precipitation: CMIP5 and multiscale global climate models comparison. Geophys Res Lett 40:5999–6003. https://doi.org/10.1002/2013GL057987
- Rugenstein A et al (2019) LongRunMIP: Motivation and design for a large collection of millennial-length AOGCM simulations. Bull Amer Meteor Soc 100:2551–2570. https://doi.org/10.1175/BAMS-D-19-0068.1
- Scheff J, Frierson D (2012a) Twenty-First-Century multimodel subtropical precipitation declines are mostly midlatitude shifts. J Clim 25:4330–4347. https://doi.org/10.1175/JCLI-D-11-00393.1
- Scheff J, Frierson DMWW (2012b) Robust future precipitation declines in CMIP5 largely reflect the poleward expansion of model subtropical dry zones. Geophys Res Lett 39:1–6. https:// doi.org/10.1029/2012GL052910



- Seager R, Naik N, Vecchi GA (2010) Thermodynamic and dynamic mechanisms for large-scale changes in the hydrological cycle in response to global warming. J Clim 23:4651–4668. https:// doi.org/10.1175/2010JCL13655.1
- Seo KH, Frierson DMW, Son JH (2014) A mechanism for future changes in Hadley circulation strength in CMIP5 climate change simulations. Geophys Res Lett 41:5251–5258. https://doi.org/ 10.1002/2014GL060868
- Sniderman JMK, Brown JR, Woodhead JD et al (2019) Southern Hemisphere subtropical drying as a transient response to warming. Nat Clim Chang 9:232–236. https://doi.org/10.1038/s41558-019-0397-9
- Tao L, Hu Y, Liu J (2016) Anthropogenic forcing on the Hadley circulation in CMIP5 simulations. Clim Dyn 46:3337–3350. https://doi.org/10.1007/s00382-015-2772-1
- Vecchi GA, Soden BJ (2007) Global warming and the weakening of the tropical circulation. J Clim 20:4316–4340. https://doi.org/ 10.1175/JCLI4258.1
- Wang J, Rossow WB (1998) Effects of cloud vertical structure on atmospheric circulation in the GISS GCM. J Climate 11:3010-3029

- Williamson DL, Blackburn M, Nakajima K et al (2013) The aquaplanet experiment (APE): response to changed meridional SST profile. J Meteorol Soc Jpn 91:57–89. https://doi.org/10.2151/jmsj.2013-A03
- Xie SP, Deser C, Vecchi GA et al (2010) Global warming pattern formation: Sea surface temperature and rainfall. J Clim 23:966– 986. https://doi.org/10.1175/2009JCLI3329.1

Publisher's Note Springer Nature remains neutral with regard to jurisdictional claims in published maps and institutional affiliations.

Springer Nature or its licensor (e.g. a society or other partner) holds exclusive rights to this article under a publishing agreement with the author(s) or other rightsholder(s); author self-archiving of the accepted manuscript version of this article is solely governed by the terms of such publishing agreement and applicable law.

